



UPPSALA
UNIVERSITET

*Digital Comprehensive Summaries of Uppsala Dissertations
from the Faculty of Science and Technology 2086*

Band gap engineering in $\text{Cu}_2\text{ZnGe}_x\text{Sn}_{1-x}\text{S}_4$ thin film solar cells

NISHANT SAINI



ACTA
UNIVERSITATIS
UPSALIENSIS
UPPSALA
2021

ISSN 1651-6214
ISBN 978-91-513-1326-9
URN urn:nbn:se:uu:diva-456779

Dissertation presented at Uppsala University to be publicly examined in Room 4001, Ångströmlaboratoriet, Lägerhyddsvägen 1, Uppsala, Friday, 10 December 2021 at 09:15 for the degree of Doctor of Philosophy. The examination will be conducted in English. Faculty examiner: Professor Edgardo Saucedo (Catalonia Institute for Energy Research).

Abstract

Saini, N. 2021. Band gap engineering in $\text{Cu}_2\text{ZnGe}_x\text{Sn}_{1-x}\text{S}_4$ thin film solar cells. *Digital Comprehensive Summaries of Uppsala Dissertations from the Faculty of Science and Technology* 2086. 84 pp. Uppsala: Acta Universitatis Upsaliensis. ISBN 978-91-513-1326-9.

Photovoltaics based on kesterite $\text{Cu}_2\text{ZnSnS}_4$ (CZTS) has attracted interest as a sustainable alternative to other thin film technologies due to their tunable material properties and earth-abundance. However, the efficiency is limited to 12.6 % for selenium-containing CZTS, with a large voltage-deficit due to tail states, deep defects, secondary phases etc.

In this thesis, Ge incorporation in kesterite solar cells was utilized to reduce Sn-related deep defects and tune the band gap. CZTS, $\text{Cu}_2\text{ZnGeS}_4$ (CZGS), and mixed $\text{Cu}_2\text{ZnGe}_x\text{Sn}_{1-x}\text{S}_4$ (CZGTS) films, and solar cells were investigated. CZGS showed wurtzite-like phases when sputter-deposited in a sulfur-rich atmosphere using GeS target. The mixture of phases could not recrystallize to kesterite phase after annealing, so, metallic Ge target was utilized for CZGTS absorber fabrication. From varying the Ge content in CZGTS, it could be concluded that CZTS grain growth increased at a low concentration of Ge.

Sulfurization of CZTS layers deposited on top of CZGS was done to achieve band gap grading. Glow Discharge Optical Emission Spectroscopy showed smooth grading while Scanning Tunneling Microscopy/Energy Dispersive Spectroscopy showed a separation between larger Sn-rich grains at the front and smaller Ge-rich grains at the back. For longer annealing times, recrystallization of the complete film was seen together with a smeared-out grading.

Germanium-rich absorbers often delaminated during the etching of the annealed samples. Adhesive TiN interlayer was used on the Mo-coated Soda-Lime Glass substrate to avoid delamination with partial success. Ge-containing samples showed oxygen-rich grain boundaries and voids. Oxide removal during etching has a possible connection to the issues with adhesion.

Solar cell performance was not improved for graded absorbers compared to CZTS. An increasing cliff-like band alignment with the buffer layer could negate the benefit of a band gap gradient since Ge diffused to the front. CZGS solar cells with alternative buffer layer were fabricated to investigate front interface improvement. $\text{Zn}_{1-x}\text{Sn}_x\text{O}_y$ (ZTO) buffer layers were deposited at various temperatures and thicknesses. The open-circuit voltage (V_{oc}) increased to 1.1 V for CZGS/ZTO solar cells; however, V_{oc} was relatively insensitive to ZTO band gap variations. The current was generally low but improved with KCN-etching of the CZGS absorber before deposition of the ZTO buffer layer. A possible explanation for the device behavior is the presence of an oxide interlayer for non-etched devices.

The backside interface recombination can be reduced using band gap grading as well with passivation layers. Therefore, ultrathin CZTS with oxide passivation layers of Al_xO_y or SiO_x on the back contact was investigated. The solar cell parameters improved with the addition of a thin oxide layer, but blocking behavior increased with passivation layer thickness.

Keywords: CZTS, CZGTS, bandgap grading, ZTO, KCN-etching, titanium nitride, solar cell

Nishant Saini, Department of Materials Science and Engineering, Solar Cell Technology, Box 534, Uppsala University, SE-751 21 Uppsala, Sweden.

© Nishant Saini 2021

ISSN 1651-6214

ISBN 978-91-513-1326-9

URN urn:nbn:se:uu:diva-456779 (<http://urn.kb.se/resolve?urn=urn:nbn:se:uu:diva-456779>)

To everyone who inspired me

List of Papers

This thesis is based on the following papers, which are referred to in the text by their Roman numerals.

- I. Englund, S., Saini, N., Platzer-Björkman, C. $\text{Cu}_2\text{ZnSn}(\text{S},\text{Se})_4$ from annealing of compound co-sputtered precursors - Recent results and open questions. *Solar Energy*, (2018) 175:84 -93.
- II. Saini, N., Larsen, J. K., Sopiha, K. V., Keller, J., Ross, N. Platzer-Björkman, C. Germanium Incorporation in $\text{Cu}_2\text{ZnSnS}_4$ and Formation of a Sn–Ge Gradient. *Phys. Status Solidi A*, (2019) 216(1900492):1-12.
- III. Saini, N., Larsen, J. K., Lindgren, K., Fazi, A., Platzer-Björkman, C. Band gap engineered $\text{Cu}_2\text{ZnGe}_x\text{Sn}_{1-x}\text{S}_4$ solar cells using an adhesive TiN back contact layer. *J. Alloys Compd.*, (2021) 880 (160478).
- IV. Saini, N., Martin, N. M., Larsen, J. K., Hultqvist, A., Törndahl, T., Platzer-Björkman, C. Record 1.1 V open circuit voltage for $\text{Cu}_2\text{ZnGeS}_4$ based thin-film solar cells using atomic layer deposition $\text{Zn}_{1-x}\text{Sn}_x\text{O}_y$ buffer layers, (2021) *Submitted*.

Reprints were made with permission from the respective publishers.

Author's contributions to the papers

- I. Mainly contributed to planning, literature review, synthesis and alloying section, figures, writing with input from co-authors.
- II. Main contribution in planning, absorber synthesis (co-sputter deposition, annealing, and etching), material characterization (XRD, Raman/PL, SEM, reflectance/transmittance, and GDOES), analysis, writing with input from co-authors.
- III. Main contribution in planning, sample preparation (co-sputter deposition, annealing, and etching), material characterization (XRD, Raman/PL, SEM, and GDOES), solar cell device fabrication (CBD, sputtering), device characterization (J-V, EQE), analysis, writing with input from co-authors.
- IV. Main contribution in planning, sample preparation (co-sputter deposition, annealing, and etching), material characterization (XRD, Raman/PL, SEM, and XPS), solar cell device fabrication (CBD, part of ALD, sputtering), device characterization (J-V, EQE), analysis, writing with input from co-authors.

Related work not included in the thesis

1. Larsen, J. K., Larsson, F., Törndahl, T., Saini, N., Riekehr, L., Ren, Y., Biswal, A., Hauschild, D., Weinhardt, L., Heske, C., Platzer-Björkman, C. Cadmium Free $\text{Cu}_2\text{ZnSnS}_4$ Solar Cells with 9.7 % Efficiency, *Adv. Energy Mater.*, (2019) 9(1900439):1-8.
2. Assar, A., Martinho, F., Larsen, J., Saini, N., Moro, M., Stulen, F., Grini, S., Engberg, S., Stamate, E., Schou, J., Hansen, O., Vines, L., Platzer-Björkman, C., Canulescu, S. Impurity gettering in polySi/SiO_x passivating contacts enabling thermally resilient Si bottom cells for tandem solar energy conversion applications, (2021) *In manuscript*.
3. Khavari, F., Saini, N., Keller, J., Larsen, J. K., Sopiha, K. V., Martin, N. M., Törndahl, T., Björkman, C. P., Edoff, M., Post-deposition sulfurization of CuInSe_2 solar absorbers by employing sacrificial CuInS_2 precursor layers, (2021) *Submitted*.

Contents

1	Introduction	13
1.1	Background	13
1.2	Thesis motivation and aim	16
2	Solar cells	18
2.1	Semiconductor fundamentals	18
2.2	Band gap of solar cell materials	20
2.3	CZTS solar cell structure and fundamentals	22
2.3.1	Substrate	22
2.3.2	Back contact and interlayer	23
2.3.3	Absorber	23
2.3.4	Buffer layer	28
2.3.5	Transparent conducting oxide front contact	28
3	Solar cell fabrication	29
3.1	Sputtering	29
3.2	Sulfurization of precursors	31
3.3	Other deposition methods	33
3.3.1	Back contact deposition	33
3.3.2	CdS deposition	33
3.3.3	$\text{Zn}_{1-x}\text{Sn}_x\text{O}_y$ deposition	34
3.3.4	Front contact deposition and scribing	34
4	Material and solar cell characterization methods	35
4.1	X-ray techniques	36
4.1.1	X-ray fluorescence	36
4.1.2	X-ray photoelectron spectroscopy	37
4.1.3	X-ray diffraction	37
4.2	Optical characterization	38
4.2.1	Raman spectroscopy	39
4.2.2	Photoluminescence	40
4.2.3	Reflectance and transmittance spectroscopy	40
4.3	Electron microscopy	41
4.3.1	Scanning electron microscopy and energy-dispersive X-ray spectroscopy	41
4.3.2	Transmission electron microscopy	42
4.4	Glow discharge optical emission spectroscopy	43

4.5	Solar cell characterization	43
4.5.1	J-V (current density-voltage) characteristics	43
4.5.2	Quantum efficiency measurement	45
5	Results and discussion	46
5.1	Structural modification of CZTS and alloying.....	46
5.2	Formation of Ge-Sn composition gradient.....	49
5.3	CZGTS solar cell devices	53
5.3.1	Delamination and insertion of an adhesive TiN interlayer	53
5.3.2	CZTS/CZGS solar cell devices.....	54
5.4	Alternative ZTO buffer for CZGS	56
5.5	Ultrathin CZTS with passivation layer	57
6	Summary of conclusions and outlook.....	61
6.1	Conclusion	61
6.2	Future work.....	63
7	Svensk sammanfattning.....	64
8	Acknowledgments	67
9	References	69

Abbreviations and symbols

IPCC	Intergovernmental Panel on Climate Change	D.I.	Deionized Water
		CBD	Chemical Bath Deposition
PV	Photovoltaic	ALD	Atomic Layer Deposition
IRENA	International Renewable Energy Agency	XRF	X-ray Fluorescence
		SLG	Soda Lime Glass
LCOE	Levelized Cost of Electricity	Mo/SLG	Mo-coated SLG
CZTS	$\text{Cu}_2\text{ZnSnS}_4$	GB	Graphite Box
CZTSe	$\text{Cu}_2\text{ZnSnSe}_4$	RBS	Rutherford Backscattering
CZTSSe	$\text{Cu}_2\text{ZnSn}(\text{S},\text{Se})_4$	GGs	$[\text{Ge}]/([\text{Sn}]+[\text{Ge}])$
CZGTSSe	$\text{Cu}_2\text{ZnGe}_x\text{Sn}_{1-x}(\text{S},\text{Se})_4$	ZTO	$\text{Zn}_{1-x}\text{Sn}_x\text{O}_y$
		AZO	2 wt % of Al_2O_3 in ZnO
CZGTS	$\text{Cu}_2\text{Zn}(\text{Ge}_x\text{Sn}_{1-x})\text{S}_4$	i-ZnO	Intrinsic ZnO
CZTS/CZGS	Bilayer of $\text{Cu}_2\text{ZnSnS}_4$ on top of $\text{Cu}_2\text{ZnGeS}_4$	GIXRD	Grazing Incidence X-ray Diffraction
CIGS	$\text{Cu}(\text{In},\text{Ga})\text{Se}_4$	PL	Photoluminescence
CBM	Conduction Band Minima	EM	Electron Microscopy
VBM	Valence Band Maxima	STEM	Scanning Transmission Electron Microscopy
E_g	Band gap energy		
E_C	Conduction band minimum energy	TEM	Transmission Electron Microscopy
E_V	Valence band maximum energy	SEM	Scanning Electron Microscopy
E_F	Fermi energy level	EDS	Energy Dispersive X-ray Spectroscopy
KS	Kesterite		
WZ-KS	Wurtzite-kesterite		
SN	Stannite	R-T	Reflectance-Transmittance
WZ-SN	Wurtzite-stannite		
DC	Direct Current		
RF	Radio Frequency		

GDOES	Glow Discharge Optical Emission Spectroscopy
UHV	Ultra-High Vac- uum
XPS	X-ray Photoelec- tron Spectroscopy
EQE	External Quantum Efficiency
J-V	Current density- Voltage
FF	Fill Factor
J_{sc}	Short-circuit cur- rent density
V_{oc}	Open-circuit volt- age
η	Solar cell effi- ciency
φ	Grazing incidence angle
α	Absorption coeffi- cient
Φ	Work function
χ	Electron affinity
d	Thickness
h	Planck's constant
ν	Frequency of light
λ	Wavelength
J_o	Dark saturation current density
J_L	Photo-generated current density
k	Boltzmann con- stant

1 Introduction

“We do not inherit the earth from our ancestors; we borrow it from future generations.” --- Anonymous

1.1 Background

The world is developing at an unprecedented pace fueled by energy-intensive technological advancement [1], resulting in the highest ever living standard and largest global economy. According to the International Energy Agency report, the primary energy sources in 2019 remain non-renewable resources such as coal, oil, and gas to meet the world’s energy demand [2], which is 0.9 percent higher than in 2018. In a nutshell, without fossil fuel consumption, mass transportation, surplus food production and supply, technological advancements, and increased life expectancy are not currently possible [1]. At the same time, overuse of fossil fuels risks long-lasting damage to the planet and the critical question now is whether the rate at which fossil fuels are being phased out of the energy supply chain is sufficient to sustain the current living standards in society. According to the Intergovernmental Panel on Climate Change (IPCC), human-induced global temperature increase (Figure 1) must be limited to 1.5-2 °C above pre-industrial levels to limit catastrophic climate change (extreme weather patterns, rising sea levels, and rising global temperature) [3]. However, unless all greenhouse gases are significantly reduced [4], limiting global warming to 1.5 °C will be impossible. Therefore, making tremendous and time-bound progress towards clean energy alternatives is crucial.

Solar energy is an abundant and virtually free source of renewable energy on a global scale. However, in the time domain, sunlight availability does not always coincide with energy demand, making solar energy unreliable without efficient energy storage and distribution technologies [5]. Current solar cell (photovoltaics, PV) technology has a decent lifespan of more than 25 years [6], and more efficient solar PV technologies are being investigated. In addition, different recycling technologies have been investigated for the last few decades [7], but the primary issue is to stay abreast of current solar cell technology. Nonetheless, there cannot be a single solution to fulfill the world’s rising energy demand. The combination of different renewable technologies (hydroelectric, wind, biomass, geothermal, tidal) together with storage can be

a better solution depending upon the geographical location, to ensure a reliable energy supply.

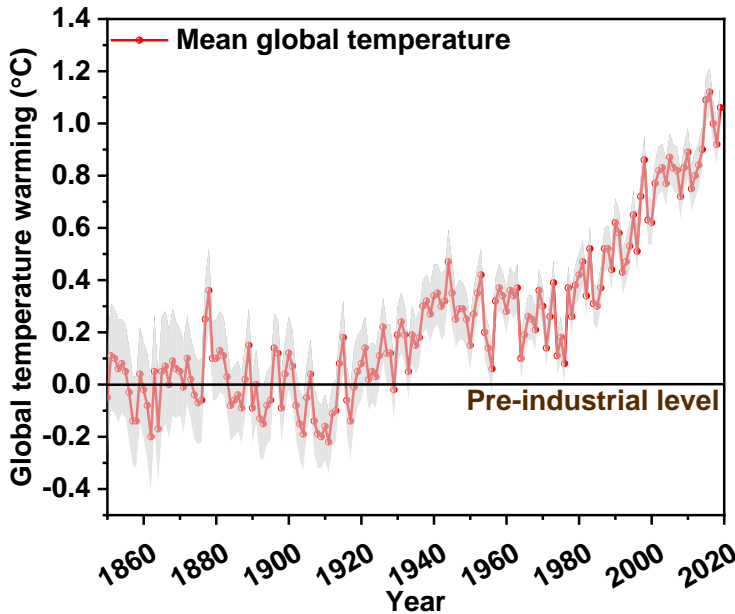


Figure 1 Global temperature rise above pre-industrial level¹. The figure is adapted from [10,11].

Solar energy is an abundant and virtually free source of renewable energy on a global scale. However, in the time domain, sunlight availability does not always coincide with energy demand, making solar energy unreliable without efficient energy storage and distribution technologies [5]. Current solar cell (photovoltaics (PV)) technology has a decent lifespan of more than 25 years [6], and more efficient solar PV technologies are being investigated. In addition, different recycling technologies have been investigated for the last few decades [7], but the primary issue is to stay abreast of current solar cell technology. Nonetheless, there cannot be a single solution to fulfill the world's rising energy demand. The combination of different renewable technologies (hydroelectric, wind, biomass, geothermal) together with storage can be a better solution depending upon the geographical location, to ensure a reliable energy supply.

Earth typically receives around 3,400,000 EJ on its surface throughout the year, which is at least 7000 times higher than annual global energy consumption [12]. In terms of practical application, on a global scale, land availability is not a concern [13]. It is slightly more challenging, particularly in densely

¹ The term 'pre-industrial levels' may refer to historical period (according to IPCC, 1850-1900) prior to the commencement of the industrial revolution [8,9].

crowded areas. According to Breyer [14], the densely populated regions can generate almost 20 % of the world's solar energy consumption. One possibility is to employ roofs and facades. Agrivoltaics, which utilizes solar roofing installed above fields, and solar panels that float on water are also gaining interest [15].

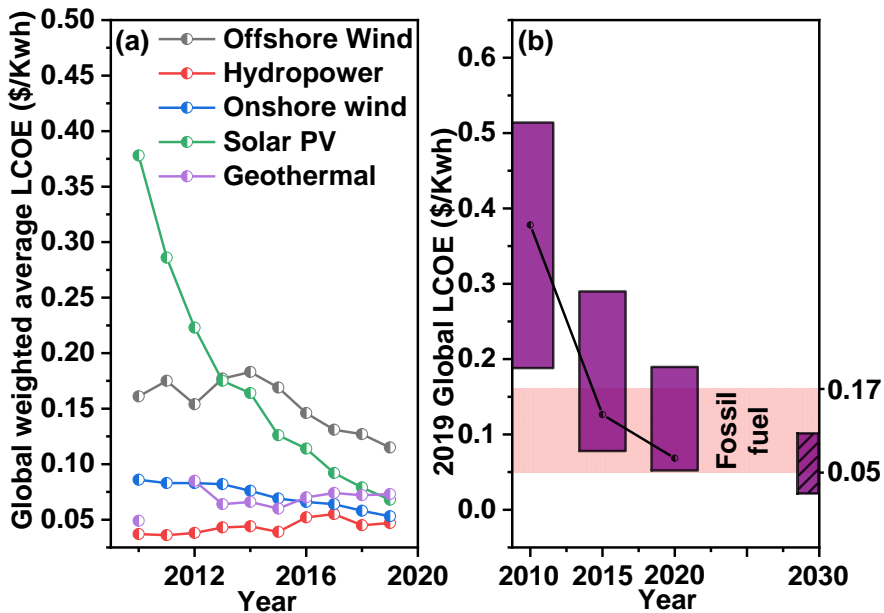


Figure 2 (a) Comparison of global weighted average levelised cost of electricity (LCOE) of solar PV with other renewable resources, and (b) LCOE forecast of solar PV and fossil fuel technology ©IRENA(2020) [16].

According to the International Renewable Energy Agency (IRENA)-2019 report [16], the renewable power mass-production stations of 2019 have generated electricity at lower costs (LCOE)² than the cheapest new fossil fuel-powered power plants (Figure 2). The net cost of the electricity generation on utility-scale solar photovoltaic prices fell steeply ($\approx 82\%$) from 2010 to 2019, making it very competitive with conventional electricity sources and other renewable sources [16]. Solar PV-generated electricity cost is slightly higher (cost reduction between 42 to 79 %) in residential sector than commercial sector, depending on the country [16,17]. According to a June 2021 report by Fraunhofer ISE [18], the operation costs (LCOE) of the solar power systems are predicted to decline continuously in comparison to traditional power plants. Renewable energy technologies are advancing at such a rapid pace that the dominating future technology is difficult to predict. However, PV cells

² Levelised cost of electricity (LCOE) is measured as the total cost of the power system per unit energy generated over its lifetime.

may become one of the cheapest and sustainable electricity generation methods in the future, since electric energy can power most of the electronic systems.

CZTS absorbers were found to have more deep defects than their Se counterpart [19–21]. The detrimental deep defects were reported to relate to the multivalence nature of Sn [22]. Ge substitution of Sn increases the band gap energy and can possibly reduce the deep defects in CZTS [22,23]. Ge incorporation in CZTSSe solar cells has been reported to give beneficial effects on device performance [24–26]. Many investigations reported Ge incorporation in CZTSSe [19,22–25,27–33], but very few studies [26–28,34,35] were conducted on the wide band gap $\text{Cu}_2\text{ZnGe}_x\text{Sn}_{1-x}\text{S}_4$ (CZGTS) investigated in this thesis.

1.2 Thesis motivation and aim

This thesis aims to explore possibilities for reduction of losses that limit performance of CZTS, by means of Ge incorporation in CZTS absorbers. This is done by fabrication and detailed characterization of CZGTS and $\text{Cu}_2\text{ZnGeS}_4$ (CZGS) thin-films and solar cells. The CZGTS or CZGS solar cell structure was taken from the widely investigated CIGS solar cells, and a two-step absorber fabrication methodology of sputter-deposition and sulfurization was used. The fabrication conditions for CZGTS are chemically more demanding than for CIGS, since the annealing condition requires high temperature and chalcogen (S or Se) overpressure [23,34]. This places great demands on the annealing atmosphere, since chemical reactions on each side of the absorber can affect the properties of the CZGS absorber. The absorber properties on the back interface can be affected, and the change in electrical properties and adhesion on back-contact can be detrimental to the performance of chalcogenide thin-film solar cells. Therefore, compositional back grading and adhesive interlayer are investigated.

In this thesis, CZGS and CZGTS absorbers were fabricated using compound sputtering and annealing. Firstly, CZGS precursors were deposited using Ge and GeS target and material properties were investigated. Then, bilayers of CZTS on top of CZGS (CZTS/CZGS) were fabricated by using co-sputtering. The development of a compositional grading was shown by varying sulfurization condition. Thereafter, adhesion of the CZGS absorber was enhanced with usage of TiN interlayer between Mo and absorber. Sulfurized CZTS/CZGS bilayers were prepared on TiN-coated Mo/SLG (TiN/Mo/SLG) to fabricate the solar cells and for their investigation. Scanning Tunneling Microscopy/Energy Dispersive Spectroscopy (STEM/EDS) of sulfurized bilayers showed fast diffusion of Ge atoms through the grain boundaries to the surface, leading to enhanced cliff-like band alignments. Therefore, alternative

$\text{Zn}_{1-x}\text{Sn}_x\text{O}_y$ (ZTO) buffer layers were deposited on CZGS absorbers with varying deposition conditions. Additionally, CdS buffer and ZTO buffers were compared for solar cells along with the effect of etching of the absorber.

2 Solar cells

A solar cell (or PV device) is a device that converts light energy into electrical energy, and semiconductors are the fundamental building block of such devices. It is essential to understand the fundamental properties of semiconductors and external factors such as temperature and dopants, affecting their properties as described in standard reference books [36–38]. Understanding the operating principle of a traditional (c-Si) solar cell is vital to comprehend new types of solar cells.

2.1 Semiconductor fundamentals

A crystalline material is composed of atoms or ions (lattice points) arranged in a periodic array in three dimensions. The array of atoms can be imagined to be divided into a smallest space (unit cell) created by a set of three planes passing through atoms, the plane in each set being parallel and equally spaced [39]. A smallest space is created by these lattice points, and such a unit cell has identical surrounding of atoms as viewed from any direction. Atoms contain a positively charged nucleus surrounded by electrons in discrete energy levels [40]. Atoms are tightly packed in a crystal so that the discrete energy level interact, resulting in allowed energy bands separated by forbidden energy gaps [41]. The bottom of the lowest unoccupied energy band and top of the highest occupied energy band are called conduction band minima (CBM (E_c)) and valence band maxima (VBM (E_v)), respectively. The difference between E_c and E_v is called band gap energy (E_g) (see Figure 3), an important parameter for semiconductor materials for solar cells. Electrons occupy the valence band, and the conduction band remains empty at absolute zero temperature. The electron occupancy of energy levels is defined by a Fermi energy level (E_f) as described in standard textbooks [36,42]. The conduction and valence band of a conductor overlaps and result in low resistivity [36]. On the contrary, the band gap of an insulator is large enough so that the conduction band is unoccupied by electrons. It should be noted that the standard band gap range for insulators or semiconductors is not clearly defined.

Semiconductor materials have a conductivity that is intermediate between conductor and insulator. In semiconductor ($E_g \approx 0.5$ to 3 eV) [42,43] materials,

the thermal energy can excite electrons to the conduction band at room temperature. If the impinging photon energy exceeds the band gap of the material, the electrons are excited from the valence band to the conduction band, resulting in free electrons. Consequently, holes are created in the valence band, resulting in electron-hole pairs. The density of holes in the valence band equals the electron density in the conduction band of an intrinsic semiconductor, as shown by the presence of Fermi level in the middle of the band gap (Figure 3). In n-type semiconductors, the Fermi energy level is located near the conduction band whereas, in p-type semiconductors, Fermi energy level is located close to the valence band, and underlying physics are described in the references [36].

The kinetic energy of holes is measured downward from the valence band, whereas that of free electrons is measured upward from the conduction band since electrons and holes are oppositely charged [42]. The free electrons in the conduction band or holes in the valence band can contribute to current flow. The charge carriers can only be collected until a specific time, called lifetime; otherwise, they recombine. The flow of charge carriers is strongly affected by their short lifetime. Therefore, an active mechanism of charge separation, the built-in electric field by a pn-junction, is used in solar cells to sustain a current flow in semiconductors.

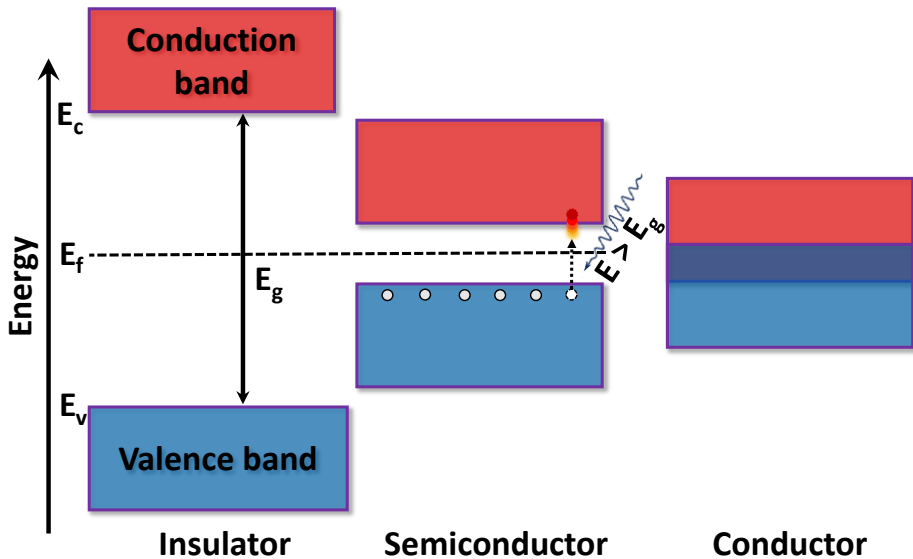


Figure 3 Schematic energy band diagram of insulator, semiconductor, and conductor. The electron-hole pairs are generated when a photon of energy greater than the band gap impinges on the semiconductor. Red solid circles represent electron in the conduction band, whereas hollow circles represent the holes in the valence band.

2.2 Band gap of solar cell materials

The band gap is an important parameter to select a semiconductor for solar cells. The photons of at least energy just higher than the band gap are required to generate electrons and holes in a semiconductor. The electrons with energy over the band gap will lose their surplus energy as heat to the solar cell, a process known as thermalization. Thermalization losses increase with a decrease in wavelength. On the other hand, the lower energy photons ($E < E_g$) cannot generate electron-hole pairs. Thus, the increasing absorption while limiting thermalization provides the theoretical limit for power conversion efficiency (PCE). Shockley and Queisser (SQ) calculated the theoretical limit of PCE for an optimum band gap based on an ideal model and certain assumptions [44]. The band gap between 1.1 to 1.6 eV was estimated to be in the optimum band gap [44]. The SQ limit is a widely used reference for understanding PV energy conversion, but many factors other than band gap energy can be considered to determine the PCE conversion limit of various solar cell materials.

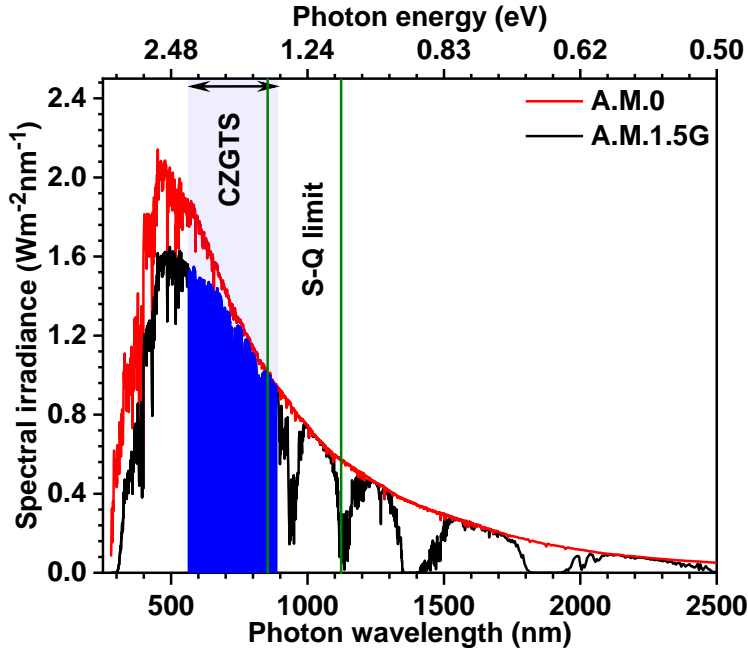


Figure 4 A.M.0 (extra-terrestrial) solar irradiance and standard A.M.1.5G solar spectrum for solar cell characterization. The band gap of CZGTS can be changed from 1.5 to 2.2 eV, as shown by blue shading. The optimum band gap is between 1.1 to 1.6 eV according to the SQ limit is marked by green line.

The solar cells are tested under standard solar spectrum, called A.M.1.5G spectrum (Figure 4). It is defined as the solar radiation traveling through 1.5 times the thickness of the atmosphere (airmass), reaching the surface of the

earth (including diffuse radiation) [45]. Sunlight consists of photons of different energy, where the distribution of energy depends upon the temperature of sun and the distance traveled by the photons through the atmosphere of the earth. Sunlight can be efficiently harvested using multijunction solar cells using the monolithic connection.

The band gap of a semiconductor can be either direct or indirect. In case of direct band gap material, the probability of sunlight absorption is higher than for indirect band gap semiconductors. The relation between thickness and absorption is given by Lambert-Beers Law,

$$I(x, \lambda) = I_o(\lambda)e^{-x\alpha(\lambda)} \quad (1)$$

where I is incident light intensity for a certain wavelength, I_o is incident light intensity, x is penetration depth below the surface, and α is absorption coefficient.

A few assumptions were made to derive the law given above, of which the most important are that the absorption coefficient and scattering losses remain constant throughout the thickness of the material [46–48]. These assumptions can be compromised in compositionally graded thin films due to variations in the mechanical properties of the films. CZGTS being a direct band gap material [49,50], a thin film of around one micron is required to absorb sunlight. A thicker layer, typically around hundreds of microns, is used for indirect band gap material, like c-Si. Therefore, thin film solar cells require less material, which can be beneficial to improve eco-friendly sustainable production. Industrial methods such as roll-to-roll production and monolithic integration can further reduce the cost of thin film solar cell technology [51]. The thin film semiconductor can be utilized in flexible solar cells, and the overall weight of solar cells can be reduced.

A pn-junction is the core of the solar cell. The separation of photo-induced charge carriers in solar cells occurs due to the electric field generated in the space charge region of a pn-junction. So, the core of solar cell is pn-junction in which conductivity changes from one type to another: p-type to n-type. The junction can be classified primarily into two types based on different semiconductors: homojunction and heterojunction. A pn-homojunction is fabricated using only one semiconductor with two regions of different conductivity types, such as in conventional (c-Si) solar cells. Two different semiconductors can be used to form a pn-heterojunction, and this type of junction is commonly used for thin-film solar absorbers as shown in Figure 6.

2.3 CZTS solar cell structure and fundamentals

Figure 5 shows the basic structure of a CZTS thin film solar cell stack. The structure includes a substrate with Mo for a back contact, p-type CZTS (or other material) as absorber, buffer layer of n-type material, and n⁺ layer as front contact layer. The function of each type of layer is described in the following sections.

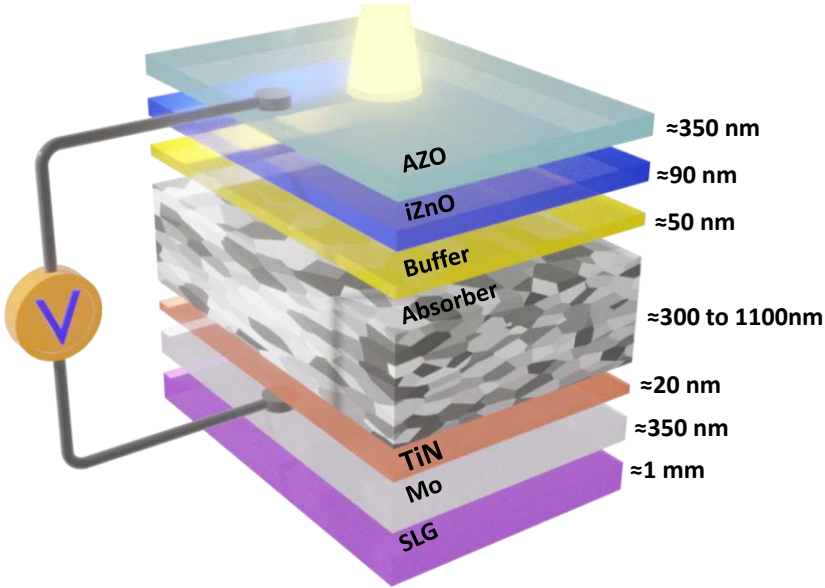


Figure 5 Illustration of the thin film solar cell stack with estimated thickness. CZGS, sulfurized bilayers of CZTS deposited on top of CZGS (CZTS/CZGS), and CZTS layers were used as absorber.

2.3.1 Substrate

A substrate is always required to support thin film solar cells. Various substrates such as steel, glass, or polymer can be chosen to deposit solar cells. The different types of substrates require different adaptations to absorber processing, e.g., taking into account the substrate's thermal tolerance, mechanical properties, and the possibility of diffusion of impurities from the substrate. The latter can be beneficial (e.g. Na from glass) or detrimental (e.g. Fe from steel) in certain cases. Soda-lime glass (SLG) is commonly used in many types of solar cells as shown in Figure 5. The diffusion of impurities such as Na from the glass substrate to absorbers is reported to be beneficial for CZTS solar cells [52]. The Na layer treatment on alternative substrates such as ZrO₂ [53] and steel [54] are reported to be beneficial for solar cell performance [52]. SLG was used as the substrate to fabricate absorbers in this thesis.

2.3.2 Back contact and interlayer

The primary role of the back contact is to collect and conduct the charge carriers through the solar cell. It is the grey-colored transition layer between the absorber and the substrate in Figure 5. There are stringent requirements for the back contact material. Firstly, the sheet and contact resistivity of the back contact should be very low. The mechanical properties of the absorber should be compatible to the back contact to avoid delamination caused by stress [55]. The back contact should be stable under the required processing conditions of the absorber fabrication, which involves the corrosive chalcogen environment during annealing.

Mo, an opaque back contact metal, is the standard back contact for CIGS solar cells and has also been adopted for CZGS or CZGTS solar cells. The physical and chemical properties of Mo back contact can change at high sulfurization temperature. Since MoS_2 grows as 2-D layered hexagonal structure with weak interlayer Van der Waals forces, the preferred growth orientation along the c-axis can lead to weak adhesion. Delamination can occur due to mechanical stress arising due to deposition conditions. In addition to this, a mismatch in the thermal expansion coefficient can cause delamination or bulging during heat treatments [56]. Adhesion can be a complex problem if stresses occur at different steps of thin film deposition.

In Paper-III, CZGS absorbers delaminated completely from Mo-coated SLG after KCN etching; however, insertion of a TiN interlayer increased the adhesion of the CZGS absorber. In the same paper, another set of CZTS/CZGS bilayer absorbers was prepared, and some of the sulfurized bilayer absorbers were delaminated after KCN etching on TiN/Mo/SLG. Owing to the partial success of TiN/Mo/SLG, its use was continued for the CZGS absorbers in Paper-IV. Additionally, the back-contact can influence the diffusion of impurities such as Na into the absorber [57,58], which could change the properties of the absorber.

2.3.3 Absorber

An absorber is the fundamental building block of the solar cell for the absorption of sunlight and power generation. In this thesis, absorbers such as CZGS ($E_g \approx 2.2\text{eV}$) and CZTS ($E_g \approx 1.5\text{eV}$) are used in ungraded solar cells. The maximum PCE of kesterite solar cells is still limited to 12.6 % [59], although the band gap of CZTS lies within the optimum range of the SQ calculations. The V_{oc} -deficit ($E_g/q - V_{oc}$) of the CZTS solar cells is often reported to be a common bottleneck for limited PCE [60–62]. The exact reason for the low V_{oc} is still debated, but band tailing, deep defects, and interface recombination are reported to be the main culprit [60,63] as discussed in Paper-I. Deep defects occur not only as a result of impurities, but also as a result of deep levels due to intrinsic defects in CZTS [64]. Sn can exist not just at its crystallographic

location but can also exist at Cu or Zn lattice sites [65] due to different structural alterations in CZTS with distinct ordering. Sn can assume a +II oxidation state at Cu site. However, Sn can assume +II or +IV state on the Zn site. The transition of oxidation state from +IV to +II state on Zn site is reported to create a detrimental deep defect [64].

Replacement of Sn with Ge can suppress the formation of deep defects to reduce bulk recombination (Paper-I) [63,66–68]. Additionally, in CZTS, the replacement of Ge has been reported to increase the grain size [26,28,66,69] and rough texture [26,28] with an increase in Ge content. The large grain size can reduce the defects along grain boundaries, which might enhance the solar cell performance. Most of the relevant studies focus on low band gap with selenium-based single junction solar cells, which left a lot of the scope for developing wide-band gap CZGTS absorber for multijunction application [70,71]. The PCE of several CZGTS solar cells is summarized in Table 1.

Table 1 Compilation of CZGTS solar cells composed of a homogeneous alloy that have been reported in the literature.

Alloying composition ([Ge]/([Sn]+[Ge]))	E_g (eV)	V_{oc} (mV)	V_{oc}-deficit (mV)	PCE (%)	Ref.
< 0.1	1.5	629	871	5.5	[72]
≈ 0.1	1.4	590	810	4.5	[73]
0.5	1.6	480	1120	4.6	[74]
0.7	1.8	870	930	2.4	[70]
1	2.0	700	1300	0.7	[28]

2.3.3.1 Homogeneous absorbers

As already described, an absorber absorbs sunlight and generates current. CZTS or CZGS absorbers are required to show good conductivity. The absorption coefficient of both absorbers is comparable. The lifetime and mobility of the charge carriers should be sufficient to facilitate the charge carrier transport through the absorber. The reported diffusion length for CZTS and CZTSe is around 500 [75,76] and 2000 nm [77], respectively. In contrast, the lifetime for CZTS [78,79] is reported to be 13 ns compared to 7 ns for CZTSe [80]. The charge carrier lifetime is reported to increase if Sn is completely replaced by Ge in CZTSe [67,81]. However, these parameters are still under research for CZGS.

Collord and Hillhouse et. al. [82] reported the improved PCE (11 %) with [Ge]/([Sn]+[Ge]) (GGS) of 0.25 due to reduction of V_{oc} -deficit. V_{oc} was found to be as high as 226 mV with GGS of 0.7 in CZTSe, however, the PCE dropped significantly with high GGS due to unfavorable band alignment between CZGTSe and CdS and formation of midgap deep defects. The best Ge homogeneous alloyed kesterite had achieved an efficiency of 12.3 % ($E_g \approx 1.2$ eV) with selenium incorporation and retained the high potential of single-junction high-quality solar cell [83]. V_{oc} -deficit (583 mV) of the selenized devices

was improved by a reduced band tailing via controlled distribution of GGS. The author also reported the improvement in charge carrier's lifetime along with the reduction in carrier recombination absorber/buffer or in the space charge region.

In the case of sulfur and selenium-containing absorbers, Ford et. al. [66] reported the 6.8 % efficient solar cell composed of $\text{Cu}_2\text{ZnGe}_x\text{Sn}_{1-x}(\text{S}_y\text{Se}_{1-y})_4$ (CZGTSSe) nanocrystals ink with GGS of 0.7. Hages et. al. [67] optimized the nanocrystal method and reported a significant device improvement up to 9.4 % in CZGTSSe solar cells with $\text{GGS} \approx 0.3$. The increased minority carriers along with reduced voltage-dependent collection were also reported by the author.

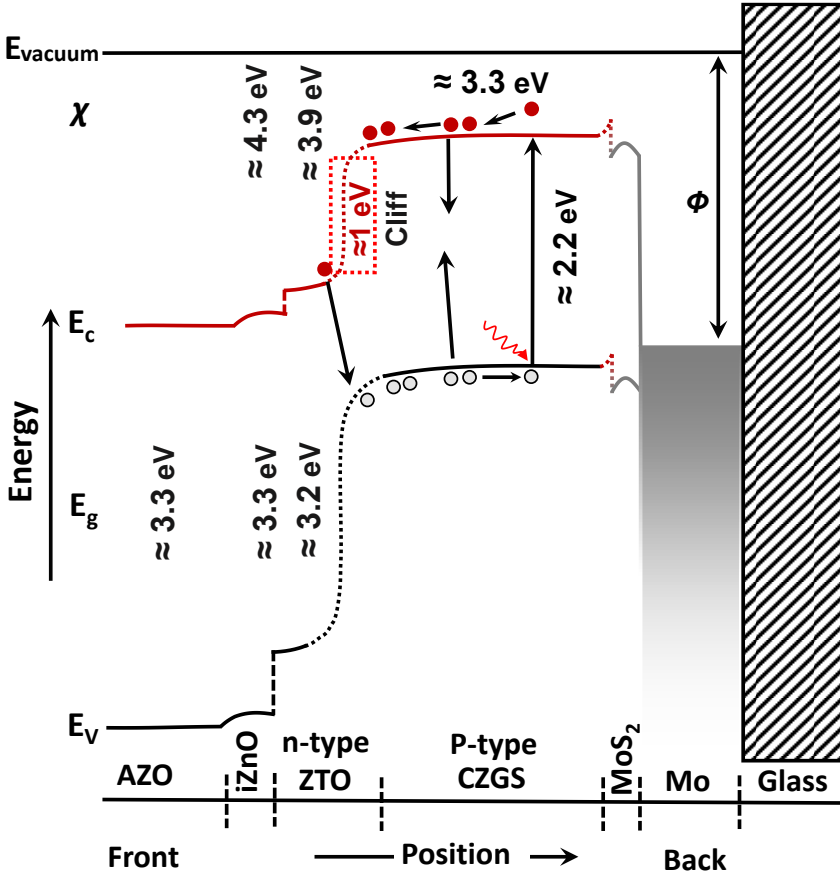


Figure 6 Schematic band diagram of thin film solar cell in which n-type ZTO buffer layer is deposited on CZGS absorber solar cell. Here χ and Φ are the electron affinity and work function [84,85].

The performance of CZGS solar cells was still limited to 0.7 % as shown in Table 1. In sulfur-containing CZGTS absorbers, the electrically and optically active defect would be critical for the application. Levchenko et. al. [86]

reported the optical properties of $\text{Cu}_2\text{ZnGeS}_4$ single crystals using Raman and photoluminescence. PL spectra consisted of two emission bands at 2 eV and more intense near 1.4 eV. The reported bands were attributed to the donor-acceptor pair transition with low activation energy for a less intensive band [86], limiting the overall device performance. Additional performance bottlenecks could occur due to non-radiative bulk and interface recombination as discussed in Paper-I.

In this thesis, CZTS and CZGS are used as ungraded absorbers for solar cells. The conduction band shifts up with increase in Ge concentration of CZTS, the band alignment between CZGS and CdS is also expected to be negative [84,85], as shown in Figure 6. Cliff-like alignment can reduce V_{oc} from optimal and increase interface recombination. However, a large spike-like alignment can block the photocurrent. Therefore, a small spike-like band alignment is desirable. On the other hand, back-contact interface recombination is also needed to be reduced which could be achieved using back surface passivation or improved band alignment.

2.3.3.2 Sn-Ge graded absorbers

Improved performances were reported by rear band gap grading of CZGTSSe compared to CZGTS. Marquez et. al. [87] reported the segregation of Ge towards the back of the absorber even though Ge was deposited on the front side of CZTSe. Andrade-Arvizu [23] reported the back band gap grading with similar methodology using different GGS of 0.2 and 0.4. The optoelectronic properties of the graded device were improved from the ungraded solar cell to the graded solar cell. The improvement in band gap graded device was attributed to improved carrier collection assisted by artificial electric field and reduction in back side recombination.

In case of sulfurized CZGTS, short-circuit current density (J_{sc}) could decrease due to the larger band gap caused by Ge inclusion in CZTS. The band gap grading could be used to compensate the J_{sc} as also discussed in Paper-I. Kim et. al. [74] reported a back-graded CZGTS solar cell fabricated by nanocrystals-based precursors. The band gap of the absorber was decreased from back side (1.85 eV) to front side (1.62 eV). PCE of graded improved from 4.6 % to 6 % (ungraded reference), due to increase in J_{sc} and V_{oc} .

Figure 4 shows the estimated band gap change in CZTS with increase in Ge incorporation. The conduction band shifts up with increase in Ge concentration in CZTS. This leads to an artificial electric field defined as conduction band gradient. Therefore, a smooth increment in conduction band from front interface to back interface can create an electric field from back interface to front interface. This electric field can push electrons from back to reduce back surface recombination. In Paper-II and Paper-III, a compositional gradient is investigated from back contact to front contact. The compositional grading of absorbers on interface can be useful to tune the interfacial band alignment. Such layer is an ideal choice to avoid carrier recombination from front or back.

However, it comes with a challenge to control process conditions to improve passivation. The passivation can usually be defined as process of controlling chemical reactions on the thin films, diffusion barriers, improve of band alignment, etc. A similar study with insulating oxide layers such as Al_2O_3 [88], SiO_2 [89] are reported to show a passivation effect for CZTS and CIGS material. These layers also control the formation of MoS_2 on back contact, diffusion of Na from SLG. However, increased thickness of an oxide layer can show the effect of blocking charge carriers in the diode. In this thesis, Al_xO_y and SiO_x layers were used on back contact of the ultrathin CZTS layer. The thickness of the oxide layers was controlled to avoid insulation of the absorber.

2.3.3.3 Absorber for tandem application

As already mentioned, monolithic integration of the solar cell can be used as cost-effective solution. A major portion of the solar spectrum cannot be utilized by a single junction solar cell. It can be a suitable method for efficient use of the solar spectrum while reducing thermalization losses and increasing absorption. Figure 4 shows the optimum band gap of solar cell for single junction solar cells. Six junction solar cells are reported to show highest solar cells efficiency, with a current PCE record of 39.2 % under A.M.1.5G illumination and 47.1 % with concentrator [90]. This strategy is quite useful to harvest solar spectrum from far infrared to UV region with the advantage of reduced thermalization losses. High band gap materials such as CZGS and CZTS can be utilized for this application. The band gap of CZTS is 1.5 eV which can be used with low band gap material. Hajijafarassar et. al. [91] has recently reported the successful monolithic integration of CZTS on bottom Si solar cell (Tunnel Oxide Passivated Contact (TOPCon) architecture). One of the significant challenges for this type of tandem solar cell is to reduce the contamination by elements of CZTS. Cu diffusion in Si can form copper silicides which lead to detrimental midgap defects in Si. TiN of thickness 10 nm has been used as an effective diffusion barrier layer. CZTS absorbers of thickness around 300 nm are fabricated on top of Si solar cell [91].

In this thesis, CZTS ($d \approx 330$ nm) is deposited on top of Si TOPCon solar cells. CZTS absorbers are fabricated by a two-step process that begins with sputtering and ends with sulfurization, as described in Chapter 3. Heat treatment is the fundamental limitation for Si solar cells due to interdiffusion causing contamination of Si solar cells. The charge carrier lifetimes are significantly affected due to the incorporation of Cu impurities in Si solar cells. TiN and p+ polycrystalline-Si (polySi) layers were used to control Cu diffusion into CZTS. CZTS was annealed for different sulfurization durations to investigate the Cu diffusion into Si solar cells.

2.3.4 Buffer layer

The selection of buffer layer is stringent in order to fabricate effective pn-heterojunctions. The interface recombination can strongly impact if interfacial defect states occur due to inferior material quality or lattice mismatch [38]. n-type CdS buffer is extensively investigated for kesterite solar cells. There are many advantages of using this layer, such as protection of CZTS absorbers from sputtering of ZnO, incorporation of Cd into CZTS films [79,92], and removal of compounds on CZTS surface. However, in addition to the bulk recombination in CZTS, the next major recombination path is front interface recombination due to a cliff-like band alignment at absorber-buffer interface [93,94]. In addition, it is advantageous to exclude the use of CdS due to hazardous Cd to the environment. Different Cd-free alternative buffers have been investigated as a possible substitute for the n-type layer in CZTS. Zn-based buffer layers (ZnO, ZnS, Zn(O,S), (Zn,Mg)O, $\text{Zn}_{1-x}\text{Sn}_x\text{O}_y$) [95–98] and In-based buffers [96,99,100] were used to optimize the front interface of kesterite based solar cells.

In this thesis, ZTO and CdS buffer layers were investigated for CZTS, CZGTS, and CZGS solar cells. Figure 6 shows the band alignment of a ZTO buffer layer with a CZGS absorber. It should be noted that the band gap of the absorber and CdS buffer layer is comparable, leaving a very small portion of sunlight to be absorbed on p-type CZGS. Therefore, wide band gap materials such as ZnS, $\text{Zn}_{1-x}\text{Sn}_x\text{O}_y$, $\text{Zn}_x\text{Ge}_{1-x}\text{O}_y$ can be used as buffer layers for CZGS absorbers.

2.3.5 Transparent conducting oxide front contact

There are mainly two requirements for the window layer. The main selection criteria for this film are wide band gap, high transmittance, low reflection losses, and lowest possible sheet resistivity. Transparent conductive oxide layers are preferred to have low free charge carrier concentration with high mobility to avoid the free carrier absorption at low wavelength [101–103]. The structure used in this work is a bilayer consisting of intrinsic (i-ZnO) and conductive Al-doped ZnO (AZO). i-ZnO is a resistive layer to avoid the shunt paths, and AZO is highly doped ZnO with low sheet resistance.

3 Solar cell fabrication

In this chapter, all fabrication protocols for solar cell fabrication are described. A two-step procedure was used throughout the thesis to produce absorber layers (CZTS, CZGS, or CZGTS) that involved co-sputtering at a low temperature (250 °C) in the first stage and a high-temperature (≈ 582 °C) sulfurization in the second stage. SLG was used as a substrate, and the other layers of the devices were deposited using Chemical Bath Deposition (CBD), Atomic Layer Deposition (ALD), and sputtering.

3.1 Sputtering

The sputtering process takes place in a chamber evacuated at low pressure, as shown in a schematic diagram in Figure 7. In the chamber, single or multiple solid material targets comprising coating elements are used in conjunction with substrates to be coated. When a high negative potential is applied to the target with a controlled supply of inert sputtering gas, the gas atoms ionize, and a plasma is generated. Sputtering is a type of physical vapor deposition method in which energetic (inert gas) ions from plasma are bombarded on the surface of a target (cathode) material, causing ejection of its constituent atoms. The ejected atoms and ions are deposited on the substrate (anode). The deposition rate depends upon the sputter yield of the target material. The sputter yield can be defined as the number of ejected atoms per incident ion, which increases with the energy and mass of the ions and depends on the angle of incidence of the ions. To deposit multi-component materials, multiple targets can be sputtered simultaneously to obtain a homogenous film of the required composition. In compound sputtering, the main advantage of sputtering is that multicomponent targets (alloys) do not change metallurgically due to thermal diffusion, chemical reactions, or back-sputtering, and the sputtering process ensures layer-by-layer ejections.

Two types of sputtering processes are used: Direct current (DC) and Radio-frequency (RF) sputtering. DC sputtering is an inexpensive technique to sputter conductive targets. However, DC sputtering cannot be used for semiconductor or insulator targets since charge buildup on the target material may eventually lead to arcing and poisoning the target material. Pulsed DC and RF sputtering are used for sputtering CuS, ZnS, and SnS targets. RF sputtering

alternates the current at radio frequency, preventing a charge from building up. This technique requires an RF power supply of 13.56 MHz with typically high power (1 to 2 kW) and about 2 kV peak-to-peak voltage to couple cathode using a matching network, adding more cost to the system.

Sputtering is a scalable industrial technique that can be used to deposit thin films over a large area. The magnetron was a significant advancement in sputtering. A magnetic field parallel to the surface of the target is introduced. The ionization efficiency is enhanced since some electrons are bound to the surface of the target by the orthogonal electromagnetic field, increasing the energy and density of ions and resulting in a high sputter rate. A tunnel-shaped magnetic field creates endless toroidal trapping zones to restrict the discharge plasma near the cathode surface. Sputtering is an energy-intensive method; however, improvements such as RF and magnetron make it versatile and efficient to deposit adherent films of high purity at low pressures.

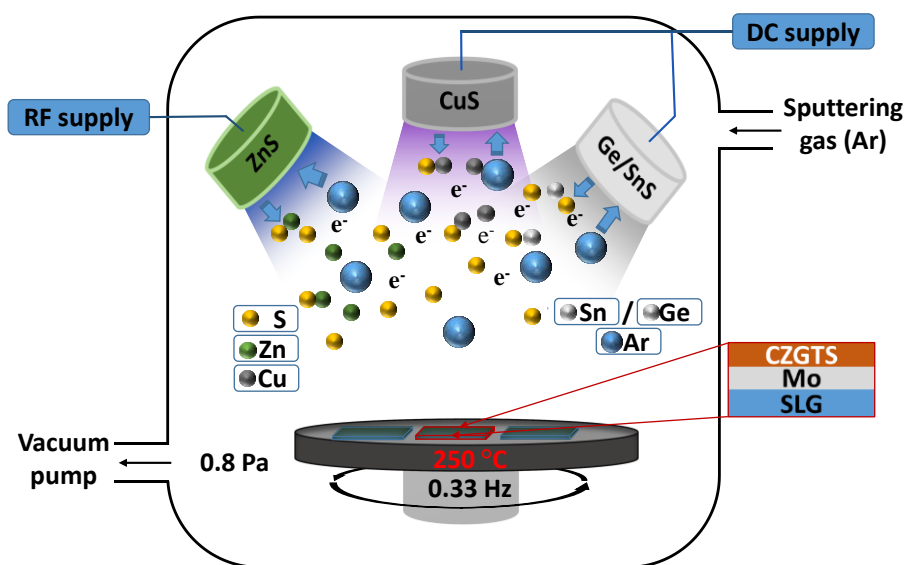


Figure 7 Schematic diagram of compound sputtering system with CZGTS precursor deposition conditions.

The sputter deposition was carried out in a controlled atmosphere of about 1 Pa of gas during this work. The gas atmosphere was comprised of non-reactive Ar (99.99 % purity) for Mo, CZGTS, i-ZnO, AZO deposition, and a combination of high purity Ar+N₂ for reactive sputtering deposition of TiN. The base pressure of different vacuum chambers was close to 10⁻⁵ Pa. CZGTS films were prepared using co-sputtering of CuS, ZnS, Ge, and SnS (all were 99.99 % pure) targets. Investigations of using GeS target instead of Ge are reported in Paper II and chapter 5. The depositions were carried out on SLG substrates coated with Mo (Mo/SLG) that had been deposited by DC sputtering of a Mo target (Paper-II). CZTS/CZGS or CZGS layers were deposited on

TiN/Mo/SLG in Paper-III and Paper-IV. CZGS films were briefly air-exposed before deposition of the second layer of CZTS to measure the composition of films from each sputter batch. Constant power mode was used to sputter deposit all the targets. The deposition was conducted with a temperature of 250°C on the substrate holder spinning at 0.33 Hz (see Figure 7). The deposition was carried out in Kurt. J. Lesker sputter system. The properties of the films can be influenced by chamber pressure and substrate holder temperature. Therefore, similar conditions were used to deposit each kind of precursor; however, the properties of the films could change due to change in the composition of the films.

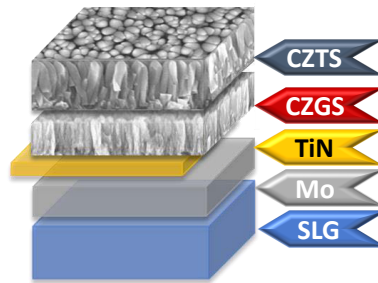


Figure 8 CZTS/CZGS bilayer precursor with an adhesive interlayer (TiN) between the absorber and Mo/SLG. This type of sample was used in Paper-III.

The adhesive TiN interlayer was deposited using Ti target (99.99 % pure) by reactive sputtering, in which reactive gas (N_2) reacts with target atoms while growing film on the substrate. Detailed information about the TiN baseline can be found in another thesis work [104]. Buffer layers were deposited on top of absorbers (sulfurized precursors). In order to finalize the solar cells, i-ZnO, AZO layers were deposited using sputtering of ZnO and AZO (99.99 % pure) targets.

3.2 Sulfurization of precursors

Sulfurization is an important process to obtain the required quality of the absorber. The best device performance is obtained from Cu-poor and Zn-rich films. A sulfur-rich annealing atmosphere can be used to control loss of excess Sn due to slow diffusion and loss in the atmosphere [105]. Insulating phase ZnS still segregate on the interfaces. Another advantage of using second stage annealing can be helpful to create a concentration gradient of Ge and Sn in CZGTS. CZTS/CZGS bilayers are fabricated before annealing in the presence of sulfur. The controlled duration of annealing can be useful to control the elemental diffusion of Ge and Sn. The grain growth and decomposition of the

CZTS phase are also controlled with sulfur, Ar overpressure, and anneal duration [106].

The absorbers are prepared by sulfurization (reacting with sulfur vapor) of a bilayer or single layer precursor. High-temperature sulfurization is a crucial step to improve the absorber quality for solar cells. This process was done in a homemade furnace setup. The furnace can be divided mainly into three parts: load-lock zone, cold zone, and hot zone. The films were loaded into a 50×50 mm² pyrolytic coated graphite box (GB) equipped with a lid containing a 3 mm diameter hole. The samples were pushed into the transition zone between the load-lock and cold zone. The hot zone was preheated to a set temperature, and the furnace was conditioned with pumping and purging Ar gas after loading samples into the transition zone. The furnace was filled with 47 kPa Ar gas before transferring samples directly from the transition zone to the hot zone. In this way, a fast-heating rate was realized, and the sample holder temperature rose to approximately 582 °C for each sulfurization batch.

The films were annealed for a short duration (13 minutes or shorter) to avoid the decomposition of CZGTS. The timer was started once the temperature of the sample holder increased up to 550 °C. The temperature of the sample holder was estimated by a thermocouple embedded into the Ti sample holder. After completion of the sulfurization duration, the sample holder was retracted to the edge of the hot zone until the temperature decreased to 200 °C. Ar gas was removed from the furnace and pumped down to base pressure (0.7 Pa). The furnace was conditioned again with continuous flow (50 sccm) of Ar (99.9 % pure) gas, and the samples were transferred to the cold zone. Once the temperature of samples dropped below 60 °C, these were transferred to the load-lock and unloaded. The composition of the CZGS was compared before and after sulfurization, and no compositional changes were measured. However, a full systematic study on CZGS decomposition as a function of annealing conditions was not done for this thesis.

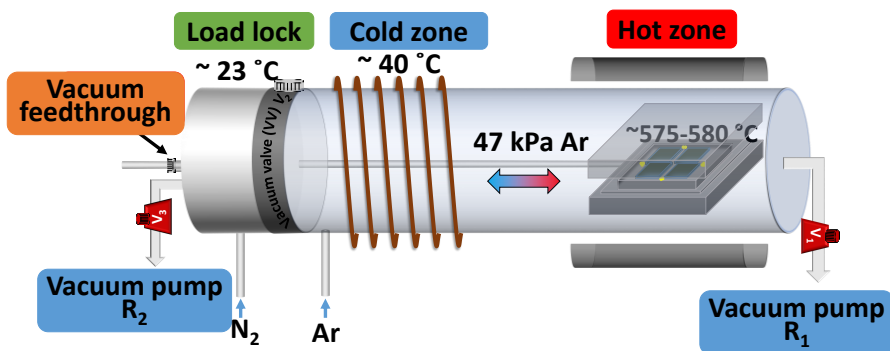


Figure 9 Sulfurization tube furnace with standard anneal conditions. The graphite box was filled with maximum of four samples and sulfur pellets, shown as yellow dots. The above figure is adapted from Paper-III.

In this thesis, 1 mm thick SLG glass was used for all the investigations. Since no diffusion barrier was used, Na was always diffused into the thin films. Glow Discharge Optical Emission Spectroscopy (GDOES) profiles of Na were compared in Paper-II and III since it can change the crystal growth of the absorber. Another study investigated the increased Na concentration owing to TiN deposition using the same baseline [104]. The standard annealing duration of thirteen minutes was used for the uniform composition of CZGTS samples in Paper-II; however, sulfurization duration was varied between two to thirteen minutes for CZTS/CZGS bilayer samples. The set temperature for the substrate holder was approximately close to 582 °C (Paper-II, III, and IV). It should be noted that the word “sulfurization” was used interchangeably with “annealing with Sulfur” throughout this thesis.

3.3 Other deposition methods

Solar cell fabrication requires a series of deposition steps from back contact to window layer deposition. This section discusses the deposition processes in detail, except for the absorber preparation, which was discussed previously.

3.3.1 Back contact deposition

Prior to cutting the substrate to $25 \times 25 \text{ mm}^2$, a baseline Mo bilayer back contact of approximately 350 nm was sputter-deposited (DC) on a $100 \times 100 \text{ mm}^2$ clean SLG substrate. The bottom and top layers were sputtered at 1500 W, with 15 mTorr for the first layer and 6 mTorr for the top layer. The sheet resistivity of less than $0.6 \Omega / \square$ was ensured for solar cell fabrication. More details about Mo deposition can be found elsewhere [107].

3.3.2 CdS deposition

Before CdS deposition, the absorbers (sulfurized precursors) were always etched in 5 wt % KCN solution for two minutes to remove secondary phases such as Cu_xS and Na compounds. The CdS film was deposited by the chemical bath deposition (CBD) method using a solution comprising 0.005 M cadmium acetate, 0.07 M thiourea, and 1.14 M ammonia. The solutions were combined in a beaker at room temperature, and the samples fitted in a stand were submerged in the same beaker. The beaker was immersed in a heated water bath at 60 °C for 8 minutes 15 seconds. The solution was stirred for 10 seconds each minute. The samples were submerged in a separate beaker of deionized (D.I.) water once the CdS deposition was completed to stop CdS growth. This method produced a thickness of approximately 50 nm CdS on CZTS [108]. CdS deposition was used in Paper-III and IV.

3.3.3 $\text{Zn}_{1-x}\text{Sn}_x\text{O}_y$ deposition

ALD is capable of producing highly conformal and pinhole-free films with precise thickness and composition control but at the expense of low deposition rate and low chemical utilization chemical usage as compared to evaporation [109,110]. ZTO buffer layers were deposited using ALD for CZGS solar cell fabrication in Paper-IV. ZTO films were deposited at 90, 100, 110, and 120 °C in a Microchemistry F120 flow reactor using N_2 (99.9999 %) as the carrier gas. $\text{Zn}(\text{C}_2\text{H}_5)_2$ (diethyl-zinc, DEZ, AkzoNobel TCO grade), $\text{Sn}(\text{N}(\text{CH}_3)_2)_4$ (tetrakisdimethylamino-tin, TDMASn, SAFC research-grade) and H_2O (D.I., 18 MΩcm) precursors were effused into the chamber as a source of Zn, Sn, and O. SnO_x and deioniz subcycles were used in 1:1 ratio. Each SnO_x subcycle was composed of TDMASn/purge/ H_2O /purge with pulse durations of 0.4/0.8/0.4/0.8 s, whereas each ZnO subcycle was composed of DEZn/purge/ H_2O /purge with pulse durations of 0.4/0.8/0.4/0.8 s. The detailed information about ZTO fabrication can be found elsewhere [111,112]. ZTO deposition was used Paper-IV.

3.3.4 Front contact deposition and scribing

A thin (90 nm) layer of resistive intrinsic zinc oxide (i-ZnO) was deposited using a radio frequency sputtering from a i-ZnO target at a pressure of 0.13 Pa Ar in Von Ardenne CS600S sputtering system. Following that, the transparent conductive layer AZO (ZnO:Al, thickness 350 nm) was deposited by RF sputtering from a ZnO:Al target (2 wt % of Al_2O_3 in ZnO). An overall sheet resistance of the combined i-ZnO/Al:ZnO layer was maintained below 40 Ω/□ on SLG for solar cell fabrication.

Mechanical scribing with a stylus was employed to define the solar cell with an area of 0.05 cm². More information about the solar cell fabrication baseline can be found in the given references [112].

4 Material and solar cell characterization methods

Material characterizations enable the understanding of fundamental characteristics of materials and monitoring of the synthesis process. Complementary material characterization methods are often needed in the case of compositionally gradient films owing to the intricacy of the material characteristics. This section will introduce the material characterization methods used in this thesis (See Table 2).

Table 2 Overview of different material characterization techniques used in this thesis. The characterization information of each technique is limited to the planned experiments for this thesis.

Method	Probe beam/method	Detection	Characterization information	Used in
Four-terminal resistivity measurement	Current and voltage	Resistivity	Sheet resistivity of back contact	Paper-II, III, and IV
XRD	X-rays	X-rays	Structure, crystallization, secondary phase	Paper-II, III, and IV
XRF	X-rays	Characteristic X-rays	Bulk composition	Paper-II, III, and IV
XPS	X-rays	Electrons	Surface composition	Paper III, IV
Raman spectra	Monochromatic light	Inelastically scattered light	Material phase, secondary phase	Paper-II, III, IV
Photoluminescence	Monochromatic light	Radiative emission	Band gap	Paper IV
Reflectance/transmittance	Wavelength dependent monochromatic light	Reflectance or transmittance	Optical band gap	Paper-II, IV
SEM/EDS	Electrons	Secondary electrons/X-rays	Morphology and qualitative composition information	Paper-II, III, and IV

STEM/EDS	Transmitted electron	Scattered electrons/X-rays	Morphology and composition	Paper-II, III
GDOES	Ar ions	Optical emission	Elemental depth profile	Paper-II, III

4.1 X-ray techniques

X-ray techniques can be extensively used for material analysis. X-ray diffraction (XRD), X-ray fluorescence (XRF) spectroscopy, X-ray photoelectron spectroscopy (XPS), Energy dispersive X-ray analysis (EDS) methods provide qualitative and quantitative information about the structure and composition of the materials. These methods are utilized to determine the chemical phases/compounds or impurities present in bulk and on the surface.

X-ray is electromagnetic radiation of wavelength range between 0.001 and 10 nm with higher penetration depth than electrons, visible light, lasers ($\lambda \approx 325$ nm to 785 nm). As a result, X-rays may provide information on the bulk properties of a material. Different types of interactions of X-rays and electrons with material relevant to this thesis are shown in Figure 10.

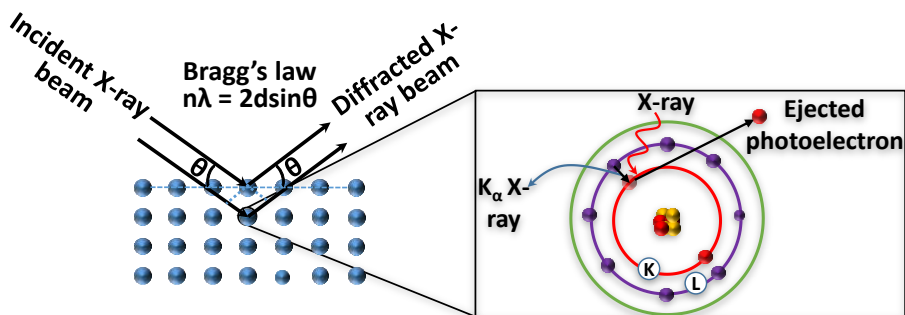


Figure 10 Interaction of X-ray with crystalline material. Characteristic X-rays generated from the material were detected for XRF measurement, and ejected photoelectrons were detected in X-ray photoelectron spectroscopy.

4.1.1 X-ray fluorescence

XRF is a quick method that generates a signal from a large portion of the sample. XRF of all the samples is measured in PANalytical Epsilon 5 setup. The diameter of the measured area on the sample is about 2 cm. X-rays have a considerably greater penetration depth than electrons; therefore, XRF has a greater information depth than EDS. The cationic composition of CZTS (CZGTS or CZGS) thin films is determined using XRF. The precursor films are always deposited onto Mo/SLG. Since Mo- L_{α} and S- K_{α} are indistinguishable, the anion composition is not quantified with XRF.

Rutherford backscattering spectroscopy (RBS) is used to calibrate the XRF measurement via a reference sample. XRF measurements of precursors were compared with the calibrated reference to determine the unknown cationic composition. XRF has been used to determine the composition of each batch in all the manuscripts. More details about the calibration process can be found elsewhere [113].

4.1.2 X-ray photoelectron spectroscopy

In XPS, an X-ray photon impinging on the material may excite an electron from the core-shell of an atom to vacuum, and the kinetic energy of the photoelectron is measured by a detector. An electron from successive outer shell (L shell) transfers to the inner shell (K-shell) and releases a characteristic K_α radiation of the atom, which is detected in an X-ray fluorescence detector. XPS is a powerful, non-destructive, and surface-sensitive technique to measure quantitative and qualitative analysis. The information depth determined by the inelastic mean free path of the excited photoelectrons is typically a few nanometers. The binding energy of each electron is calculated from the measured kinetic energy of the emitted electrons as given below,

$$E_{kinetic\ energy} = h\nu - E_{binding\ energy} - \Phi \quad (2)$$

where $h\nu$ is the energy of the X-ray photon and Φ is the spectrometer work function.

The obtained binding energy spectra are compared with references. The binding energy spectra of each element are unique and dependent on bonding with other elements (chemical environment). In this work, XPS spectra of the thin films were measured using Quantum 2000 ESCA microscope (Physical Electronics) using a monochromatic Al K_α (1486.7 eV) source. Ultra-high vacuum (UHV) (less than 10^{-5} Pa) was achieved after loading the sample inside the main chamber. The probe size of the sample was about 200 μm . The samples were air-exposed while transferring samples from the vacuum storage to the XPS UHV chamber.

4.1.3 X-ray diffraction

X-ray diffraction is a technique to determine the structure of crystalline materials. Constructive interference of a monochromatic beam of X-rays scattered at specified angles from each set of lattice planes in a film produces XRD peaks. The atomic locations inside the lattice planes influence peak intensities. As a result, the XRD pattern serves as a fingerprint of periodic atomic configurations in a material. A monochromatic X-ray (Cu K_α source ($\lambda = 1.5406 \text{ \AA}$))

incident on the material and scattered elastically from atomic planes with interplanar spacing d (see Figure 10). According to Bragg's law, X-rays reflect with constructive interference at various angles,

$$2d \sin\theta = n\lambda \quad (3)$$

Here d is interplanar spacing, λ is the incident wavelength of X-rays, θ is the incident angle between material and incoming beam, and n is an integer.

XRD is commonly used in two configurations: Bragg-Brentano (θ - 2θ) and grazing incidence. For Bragg-Brentano mode, the X-ray source tube is locked in place while the sample holder and detector are rotated so that the incoming beam incidents at θ (incident angle) and the detector is always at 2θ (angle difference between incident and reflected beam). This arrangement enables the detection of a high-intensity beam diffracted from crystalline planes situated up to a few micrometers (μm) depth in the sample. It can be used to find the preferred grain orientation. The structure of a material may be investigated using another configuration called grazing incidence X-ray diffraction (GIXRD) at different penetration depths. A parallel monochromatic X-ray beam incident at a low angle (angle greater than critical angle) and detector record signal from the diffracted beam. The beam scattering volume increases at a low incidence angle, which enhances the diffracted beam intensity for the thin film sample. The incident X-ray beam depth can be varied by varying incidence angles. Thus, in theory, GIXRD may be used to depth profile crystalline samples with low roughness.

In this thesis, Siemens D5000 was used to measure GIXRD diffractograms. It was used to determine the absorber phase, secondary phases in Paper-II, III, IV. GIXRD diffractograms of CZGTS were measured at different grazing incidence angles (0.5 to 10°) within a small 2θ range. All GIXRD measurements in $70^\circ > 2\theta > 10^\circ$ range were taken at grazing incidence of 1° . CZGTS exists as either a kesterite or stannite polymorphs (indistinguishable by XRD). The secondary phases such as Cu_xS , ZnS , $\text{Zn}_{0.5}\text{Ge}_{0.25}\text{S}$, Cu_2GeS_3 , Cu_2SnS_3 were tough to be distinguished due to XRD peak overlap at low concentration of Ge in CZGTS. ZnS and Cu_xS can be identified in CZGS material using XRD. The measured GIXRD diffractograms were verified by matching with reference patterns from ICDD. XRD peaks shifts related to the increase in Ge concentration in CZTS were measured. The presence of secondary phases was verified with other techniques such as Raman spectroscopy and STEM/EDS.

4.2 Optical characterization

An optical characterization is an essential tool for investigating fundamental semiconductor properties and device performance. The optical properties of a material can provide significant information about its physical properties,

such as thickness and refractive index. The use of spectroscopy can provide useful information about the electronic characteristics of the material. Absorbance/transmittance, photoluminescence, and Raman scattering measurements are some of the most used optical characterization techniques in this thesis. Raman and PL measurements of all the samples were carried out in the Renishaw inVia system.

4.2.1 Raman spectroscopy

Raman spectroscopy is used to determine the crystal structure and quality of the semiconductor material. It is a fast and non-destructive tool based on inelastic scattering of light. The incident light can be scattered either elastically or inelastically by the sample.

Raman spectroscopy measures the vibrational spectra of the material. The characteristics of Raman vibrational spectra of each material depend upon the mass and bonds of the neighboring atoms. Raman spectra of different materials are unique fingerprints of materials but may need references for unknown complex samples.

In Raman spectra of solid-state materials, an incoming photon excites an electron to a high energy level due to inelastic scattering. The excited electron generates or absorbs a phonon. The excited electron recombines by emitting a photon equivalent to the energy difference of excited and ground energy levels. The monochromatic laser is required to excite the electrons to precisely generate and measure the unique Raman signal.

Inelastic Raman scattering is an infrequent event in comparison to elastic Rayleigh scattering, occurring an order of million times less often [114]. Elastic Rayleigh scattering occurs when the scattered light has the same frequency as the incoming radiation. Stokes lines occur when the frequency of incoming radiation is greater than the frequency of scattered radiation. However, when the incoming radiation frequency is less than the scattered radiation frequency, anti-Stokes lines emerge in the Raman spectrum. Additionally, strong Raman signals of specific vibrational modes can be measured when the wavelength of incident radiation is close to the electronic band gap of the semiconductor. This type of Raman scattering is called resonance Raman scattering [115]. The resonance Raman scattering signal is enhanced by order of between 10^2 to 10^6 compared to ordinary Raman spectroscopy.

Multiwavelength (325, 532, 633, and 785 nm) Raman spectra of the CZGTS samples were measured for Paper-II and III. It should be noted that the penetration depth depends upon wavelength and material properties. The penetration depth of the sample is inversely proportional to the absorption coefficient of the material. A low power density (50 W/cm^2) was used for Raman measurement to avoid thermal damage. Near-resonant Raman spectra of the samples were measured with an excitation wavelength of 785 and 325 nm laser to investigate cation order-disorder and secondary phases.

4.2.2 Photoluminescence

Photoluminescence (PL) is an optical phenomenon in which semiconductors emit radiation due to radiative transition in band-to-band, or band-to-defect state, or donor-acceptor pair transition. The excited electron-hole pairs are generated by absorption of radiation of energy more than the semiconductor band gap. CZGTS is a complex material due to the presence of deep defects, defects complexes, and secondary phases. In all our studies, PL spectra of the CZGTS were measured at room temperature. At room temperature, CZTS material was reported to have tail-to-tail and tail-to-band transition in addition to the band-to-band transition [116].

4.2.3 Reflectance and transmittance spectroscopy

Absorbance can be measured indirectly using an expression $A = 1 - R - T$. The absorption coefficient [117] is determined using the equation (4) after measuring the reflectance (R) and transmittance (T),

$$\alpha = \frac{1}{t} \ln \frac{1 - R^2}{T} \quad (4)$$

Where α is absorption coefficient, t is the thickness of the film, R is reflectance, and T is the transmittance of the thin film. Equation (4) is only valid for materials with high absorption coefficient, and multiple scattering within thin film is neglected. The optical band gap of the thin film can be estimated by Tauc's plot [118],

$$\alpha \propto \frac{(h\nu - E_g)^n}{h\nu} \quad (5)$$

where α is energy-dependent absorption coefficient, ν is the frequency of light, h is Planck's constant, $n = 2$ for indirect band gaps and $n = 1/2$ for direct band gap semiconductor [118,119].

The wavelength-dependent transmittance and reflectance spectra were obtained using a PVE300 system, which includes an integrating sphere and a monochromatic light source. A monochromator was used to transform white light produced by xenon and halogen lights into monochromatic light. The integrating sphere collected the reflected intensity of direct and diffuse scattering of light. The spectra were recorded using a Si/InGaAs detector with a spectral range of 300–1700 nm. The band gap of CZTS is expected to increase with an increase in Ge incorporation. Tauc's plots were generated by plotting

$(\alpha h\nu)^2$ against photon energy ($h\nu$), and the linear region was extrapolated to the abscissa ($h\nu$ -axis) to confirm the direct optical band gaps of different alloys of CZGTS.

4.3 Electron microscopy

The resolution of the optical image is mainly limited due to the wavelength of incident radiation as defined by Rayleigh criterion [120]. The wavelength of the light used in a microscope is between ≈ 400 to 700 nm, leading to image resolution up to $\approx 0.2\mu\text{m}$. However, for electron microscopy, the imaging resolution can be significantly improved to below 0.08 nm with advanced aberration correction [121]. Therefore, electron microscopy (EM) is a technique to obtain high-resolution morphological image of a specimen. The need for sample preparation depends upon the nature of the investigation and the type of electron microscopy. In this technique, an electron beam incident on the sample, and a secondary or transmitted electron beam is detected using an inlens detector or BSD for imaging. Type-I secondary electrons (SE1) are emitted at a high angle (angle between emitted beam and sample surface) close to the impact site, carrying high-resolution, surface-sensitive (topographic) information about the material. Type-II secondary electrons (SE2) are produced from a larger volume and higher depth than SE1 electrons and are emitted from sample at a lower angle. Additional techniques such as back scattered electron detection (BSD), and EDS can be used in conjunction with SEM to probe the chemical composition the sample.

4.3.1 Scanning electron microscopy and energy-dispersive X-ray spectroscopy

Scanning electron microscopy (SEM) may require minimal sample preparation depending on the conductivity of the thin films. Secondary electrons (SE1 and SE2) are commonly used to show the morphology and topography of the samples with a nanoscale resolution by scanning an electron beam in a raster pattern across the surface of the sample.

In the case of EDS, a primary electron beam hits the core-shell (K-shell) and excites an electron to the vacuum level. A characteristic X-ray is generated when one electron from an outer shell transition to the core-shell. The characteristic X-rays of each element have a specific energy, which are detected using EDS detector. The resolution of EDS depends on the interaction volume generated by the energetic primary electron beam and material. The interaction volume increases with the increase in energy of the incident electron beam. The accuracy of EDS additionally depends on conductivity, morphology, homogeneity of the material, and overlap of characteristic X-ray

lines. For instance, Mo and S cannot be differentiated by EDS. Despite some limitations, EDS is an essential technique for qualitative compositional analysis.

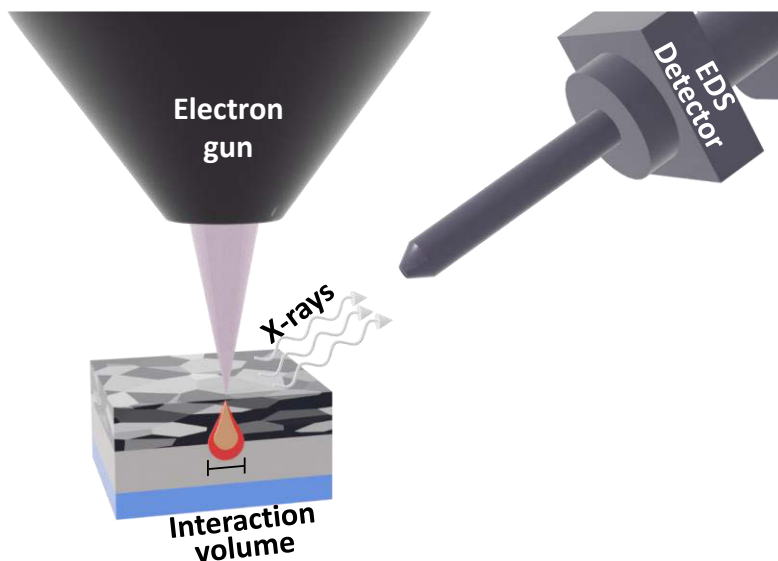


Figure 11 Interaction of primary electron beam with material and detection of characteristic X-ray of elements with EDS detector. The interaction volume of the material increases with increase in accelerating voltage of primary beam of electrons.

SEM of all the samples was done in Zeiss Leo 1550 system for Paper-II, III, IV. The imaging of the samples was done at a low accelerating voltage (5 kV) to improve the imaging details of surface morphology (in Paper-III); however, higher accelerating (15 kV) was used to measure the EDS spectrum (in Paper-II). The insulating ZnS secondary phase could be confirmed due to its bright contrast (in Paper-II). SEM imaging can be strongly affected by charging in low-conductivity samples.

4.3.2 Transmission electron microscopy

Additional sample preparation is required for TEM analysis. There are mainly two ways to prepare samples: mechanical grinding of the thin films and thin film lamella preparation by sputtering energetic ions. In a focused ion beam (FIB), ions are usually accelerated between hundreds of volts to 30 kV, where a high energy beam is used for rough milling, and low accelerating voltage is used to polish the final lamella. Thin-film lamellae were used to imaging and EDS of the samples in STEM mode. In this mode, the microscope lenses are changed to STEM mode to produce a focused convergent electron beam at the lamella surface. The lamella is scanned with beam and X-ray signals were

recorded from different elements. The point-by-point scanning generates a complete image of different elements. Thus, electron beam is focused on a narrow spot in STEM mode compared to conventional TEM imaging. The accuracy and resolution of EDS spectra significantly improve in STEM configuration. STEM/EDS has been used in Paper-II, III to measure compositional mapping of sulfurized CZTS/CZGS samples. The secondary phases in addition to the voids, were investigated on the cross-sectional morphology of thin films.

4.4 Glow discharge optical emission spectroscopy

Glow discharge optical emission spectroscopy (GDOES) is a destructive technique to measure the elemental composition from the surface to the depth of solid materials. This technique is rapid and highly sensitive to different elements and is used for qualitative and quantitative analysis. The sample is sputtered by Ar ions while using the sample as cathode, and glow discharge plasma is simultaneously detected by optical emission spectroscopy of elements. Due to the impact of variable sputter rates in various materials, matrix effects, and layer roughness, it is not easy to rely on GDOES profiles across the interfaces of multi-layered films.

In this work, the elemental composition profile of films was determined using a Spectruma Analytik GDA750HR analyzer using Ar as the sputtering gas and a 2 mm probe diameter. GDOES was done to verify observed gradient profiles, which were used to compare the qualitative distribution of different elements throughout the thickness of the absorber.

4.5 Solar cell characterization

Solar cell characterizations are essential techniques to estimate the device performance. The devices are intended to be used under sunlight which varies widely with intensity, temperature, and spectrum. Solar cells are characterized under standard operating conditions to ensure allow comparison.

4.5.1 J-V (current density-voltage) characteristics

JV measurements were done by contacting the front (n-side) and back (p-side) contacts and measuring the output current while sweeping the voltage applied to the cell, often called bias, over the desired voltage range, typically from a negative to a positive voltage (reverse bias to forward bias). The measurement is conducted in the dark first, followed by an A.M.1.5G illumination measurement. This enables the identification of light-induced effects, but the extrac-

tion of device performance parameters is performed from the light measurement, as explained by Hegedus and Shafarman [122]. Ideal J-V curves are defined by the diode equation derived from the one-diode model, which is an equivalent circuit for an ideal solar cell, as defined in Equation (6),

$$J = J_o e^{\left(\frac{qv}{nKT} - 1\right)} - J_L \quad (6)$$

Where J_o is the dark saturation current density, and a measure of recombination in the device, n is the ideality factor, k is the Boltzmann constant, J_L is photocurrent, and T is the temperature. The above parameters may be acquired by fitting the curve or a portion of it, most often to a one-diode model; however, some assumption and caution should be taken while fitting solar cells with low efficiency and non-ideal behavior [122].

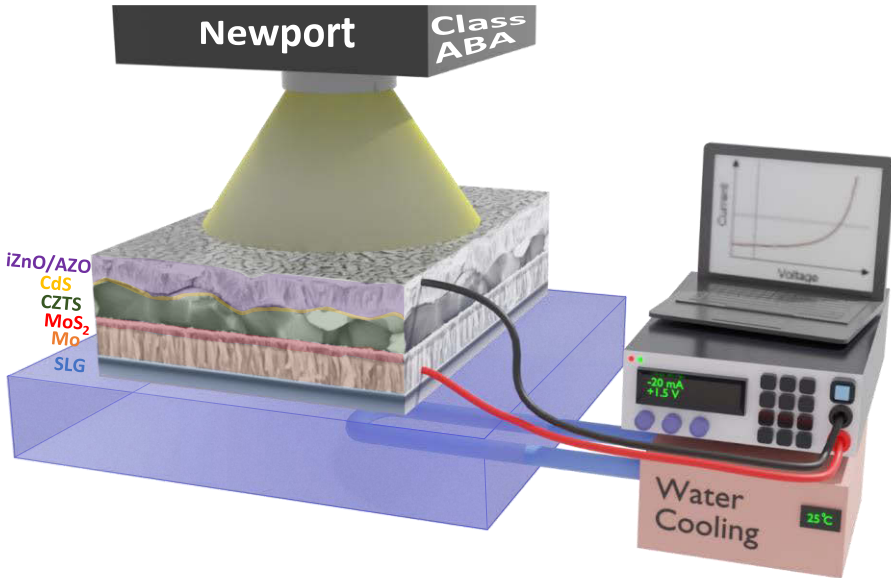


Figure 12 Schematic diagram of a CZGS solar cell illuminated for J-V measurement.

J-V measurements of the fabricated solar cells were conducted with irradiation by A.M.1.5G spectrum (1000 W/m^2) under normal temperature (25°C) and atmospheric pressure. The measurements were performed in a A.M. 1.5 solar cell simulator (Newport class ABA setup with Keithley 2401 source meter). A Xe arc lamp with A.M. 1.5 filter was used as the light source. The spectrum of the Xe arc lamp is slightly different from real A.M.1.5G solar spectrum. The lamp was turned on at least 30 minutes before measurements to ensure the stable intensity of light. The intensity of the lamp is then calibrated with known J_{sc} derived from QE measurement of reference solar cells.

The calibration could be done with a change in distance between solar cell and lamp. However, J_{sc} of the solar devices of different band gap could be affected due to a mismatch between A.M.1.5G spectrum of lamp and ideal solar spectrum.

4.5.2 Quantum efficiency measurement

Quantum efficiency is defined as ratio of output current at given wavelength and incident photon flux as given below,

$$QE(\lambda) = \frac{J_{out}(\lambda)}{q\Phi_{in}(\lambda)} \quad (7)$$

where J_{out} is output current at a given wavelength and Φ_{in} is incident photon flux at a given wavelength.

It can be categorized into two types: External quantum efficiency (EQE), where reflection losses and shading losses are taken into account, and Internal quantum efficiency (IQE), where only absorbed photons are only taken into consideration. QE is routinely used to characterize the photocurrent and the losses that contribute to the reduction of the J_{sc} . As previously stated, incoming photons of various wavelengths are absorbed in varying depths, which allows for some degree of pinpointing the depth and specific portions of the solar cell responsible for a particular loss. The photocurrent can be calculated by integrating the product of photon flux in the A.M.1.5G spectrum and the EQE at all wavelengths as given in the following equation,

$$J_L = q \int_0^{\infty} \Phi_{AM1.5G}(\lambda) EQE(\lambda) d\lambda \quad (8)$$

EQE of the samples is measured in a homemade setup calibrated by externally measured Hamamatsu Si and InGaAs solar cells. A Stanford Research Systems SR570 current preamplifier and two SR810 and SR 830 lock-in amplifiers were used to detect current and monochromatic light intensity in the EQE system. EQE measurements were done under nearly dark conditions; however, QE measurement with voltage or light bias can also be used to investigate the non-ideal solar cell devices.

5 Results and discussion

5.1 Structural modification of CZTS and alloying

In this study, CZGS precursors were sputtered deposited using Ge and GeS targets. The preparation of CZGS absorbers using Ge target was used for fabrication of CZGTS alloy with different concentrations of Ge.

CZGS is reported to crystallize into two distinct cation-ordered crystal structures: low-temperature tetragonal and high-temperature metastable wurtzite [123]. CZGS transitions from the tetragonal phase to the orthorhombic phase at a high temperature (≈ 790 °C) [124]. Different synthesis techniques have been used to synthesize the metastable wurtzite CZGS phase at low temperatures, even if it is thermodynamically unstable [124–126]. Sputter deposition of precursors can be a highly non-equilibrium process that can produce a mixture of metastable phases.

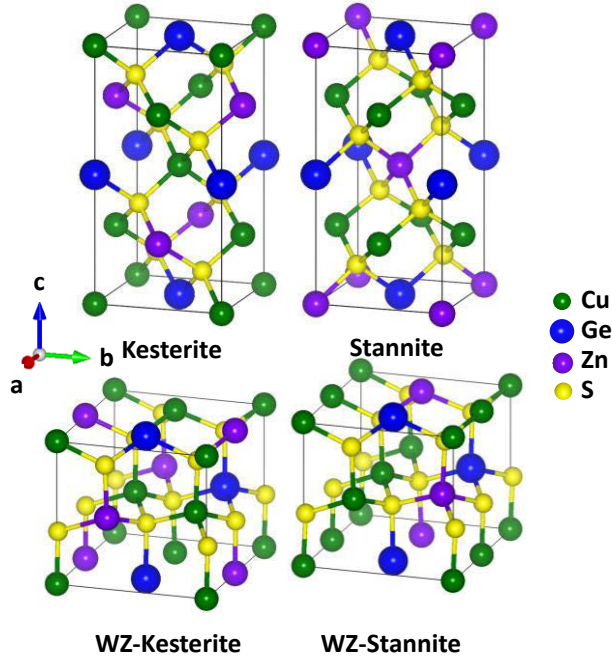


Figure 13 Crystal structure of CZGS absorber. The structure is plotted with VESTA software and the data is adapted from Paper-II [34].

In paper-II, two types of CZGS precursors were prepared by magnetron co-sputtering using two different Ge targets: elemental Ge and GeS target. CZGS precursors deposited with the elemental Ge target showed improved crystallinity and grain growth after annealing; however, those made with the GeS target showed an unknown broad peak ($40 < \theta < 60^\circ$) in GIXRD (see Figure 14).

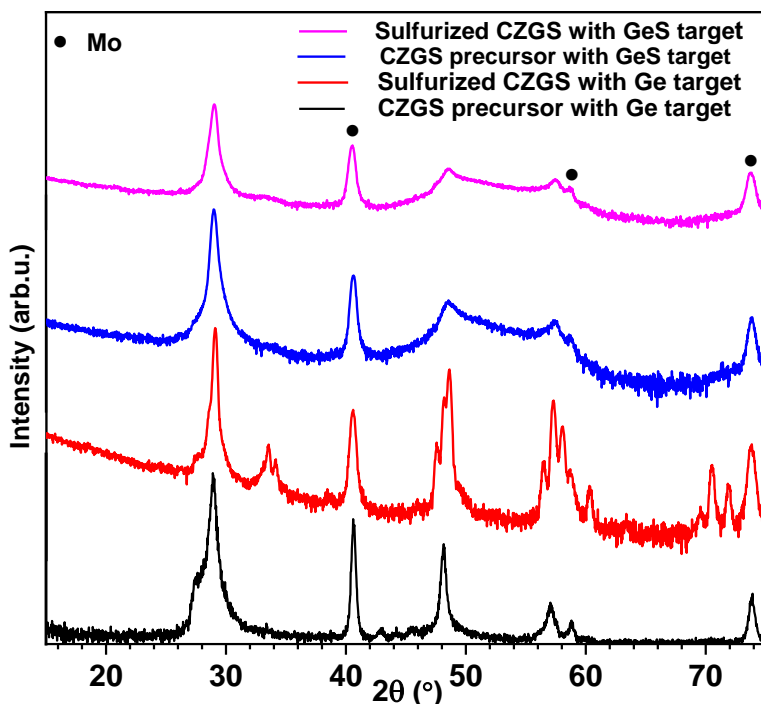


Figure 14 GIXRD of precursors and sulfurized CZGS fabricated using GeS target and Ge target. The figure is adapted from Paper-II.

To gain further understanding, the enthalpy of mixing of KS (Kesterite), Stannite SN (Stannite), WZ-KS (wurtzite-kesterite), and WZ-SN (wurtzite-stannite) phase (Figure 13) was calculated for varying Ge content of CZGTS (See Paper-II for first principle calculation) [34]. The energy difference between different phases was small, which may imply the concurrent growth of orthorhombic and tetragonal structures under non-equilibrium deposition conditions (See Paper-II). The formation energy of the KS phase was the lowest compared to other phases (SN, WZ-KS, and WZ-SN), which is consistent with previously reported studies. However, the energy difference between WZ-KS and SN is lower for CZGS compared to CZTS. The WZ-KS and KS phases must be separated by an energy barrier [127], which is greater for phases with different lattice symmetries, stabilization of the WZ-KS phase may slow down the recrystallization process [34]. So, recrystallization of sulfurized precursors could be affected due to the formation of WZ-like phases (See Figure 14).

Higher sulfur content due to GeS target was likely to support the formation of the wurtzite-like phase (See Figure 14).

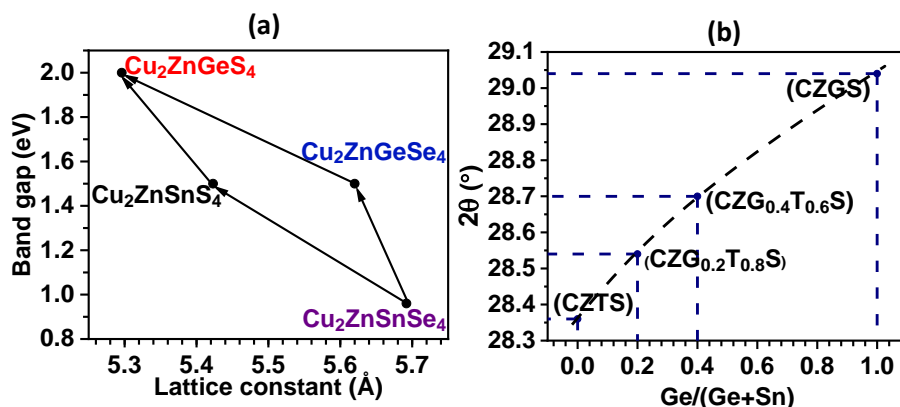


Figure 15 (a) Band gap shift with a lattice constant (Paper-I). The figure is adapted from Chen et. al. [28], Khadka et. al. [31], and Paper-I (b) 2θ shift with change in Ge concentration in CZTS. The data is taken from Paper-II [34].

Based on this, sulfur-deficient sputtering conditions were used (Paper-II and Paper-III) to deposit CZGS precursors to avoid developing a wurtzite-like phase and to improve crystallinity. In addition to this, the lattice parameter of CZTS contracts with increasing Ge concentration due to the small size of Ge atom compared to Sn, resulting in XRD peak shift (Figure 15) [28,34,123]. CZGTS absorbers were prepared using co-sputtering of CuS, SnS, Ge, and ZnS. The concentration of Ge was controlled by varying applied power to Ge and SnS targets. CZGTS absorbers were found to be recrystallized as kesterite with no clear indication of secondary phases in GIXRD. The sulfurization of CZGTS leads to the segregation of phases such as ZnS in the cross-section of CZGS. The grain size and crystallinity of the CZTS increased at low concentration of Ge in CZTS (Figure 16), which was also confirmed by other reports [128].

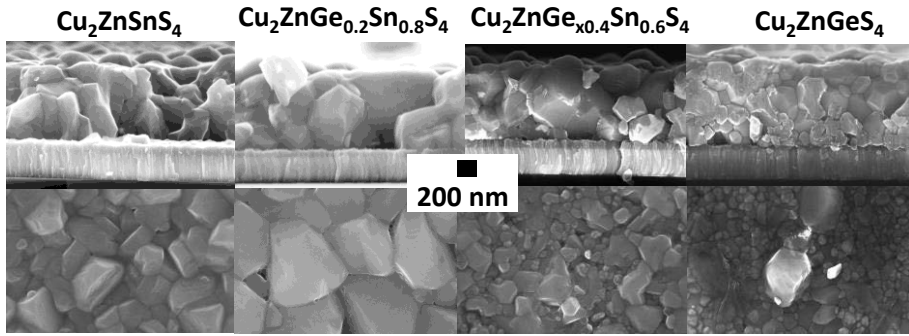


Figure 16 SEM morphology of CZTS with different concentration of germanium. This data is taken from Paper-II [34].

The formation of secondary phases such as GeO_x , ZnS , were investigated. The appearance of the insulating ZnS phase was confirmed by bright charged particles on the surface of CZGS (Figure 16) in addition to the resonance Raman spectroscopy using 325 nm laser (Paper-II, III). STEM/EDS confirmed ZnS in Paper-II and Paper-III; however, GeO_x could not be confirmed by GIXRD and Raman spectroscopy. Other phases like Cu_xS and GeO_x could be seen as Cu-rich and Ge-rich surfaces respectively by STEM/EDS (See Figure 19); however, $\text{Zn}_{0.5}\text{Ge}_{0.25}\text{S}$, Cu_2SnS_3 , and Cu_2GeS_3 might form but could not be distinguished.

5.2 Formation of Ge-Sn composition gradient

The development of band gap grading due to a depth-wise change in composition has been a vital methodology to improve device performance in chalcogen-based solar cells [129–132]. Ge substitution in CZTS has been particularly interesting for reducing Sn-related deep defects [23,24,74,130] as described earlier. The substitution of different elements has been employed in CZTS aiming at band gap engineering (Paper-I). According to theoretical investigations on Ge substitution in CZTS, the conduction band minima (CBM) form due to the hybridization of Sn-5s and S-3p in CZTS. The substitution of Sn-5s orbital with Ge-4s antibonding orbitals enhances the antibonding character of the CBM due to repulsion between s-s, and s-p orbitals of Ge and S, leading to upshift in CBM. The valence band maxima (VBM) remains unaffected due to the participation of Cu-3d and S-3p orbitals [31,69,133].

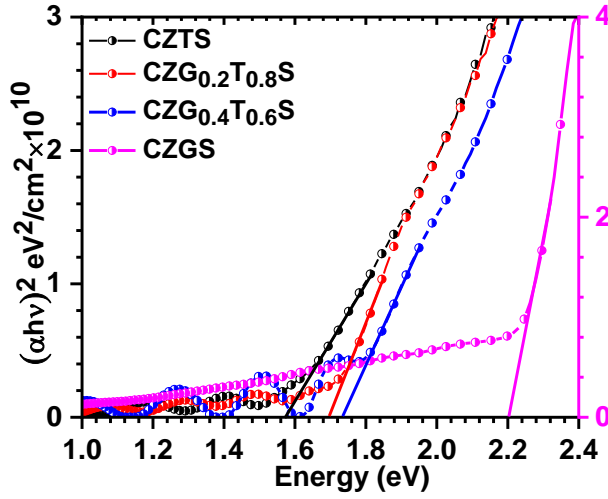


Figure 17 Tauc's plot of CZTS with different concentrations of Ge. The data is adapted from Paper-II [34].

Figure 17 shows that the band gap of CZTS increases with an increase in the concentration of Ge. Due to the possibility of good miscibility with band gap adjustment in the CZGTS alloy, it can be utilized to counteract the interface recombination in solar cell devices. In paper-II, a bilayered structure consisting of a CZTS/CZGS was co-sputter deposited on Mo-coated glass (Mo/SLG) substrates. CZTS/CZGS bilayers were annealed in a time-resolved manner at a fixed temperature. The intact layers of CZGS and CZTS vanished with an increase in anneal duration due to intermixing of Ge and Sn rich phases. Small Ge-rich grains assembled at the rear interface with larger Sn-rich grains at the front interface, forming a compositional gradient at a short anneal duration. The interdiffusion of Ge and Sn increased with long anneal duration, leading to complete intermixing of individual layers of CZGS and CZTS. This is consistent with the Raman shift of CZTS/CZGS bilayers with an increase in sulfurization duration (See Figure 18).

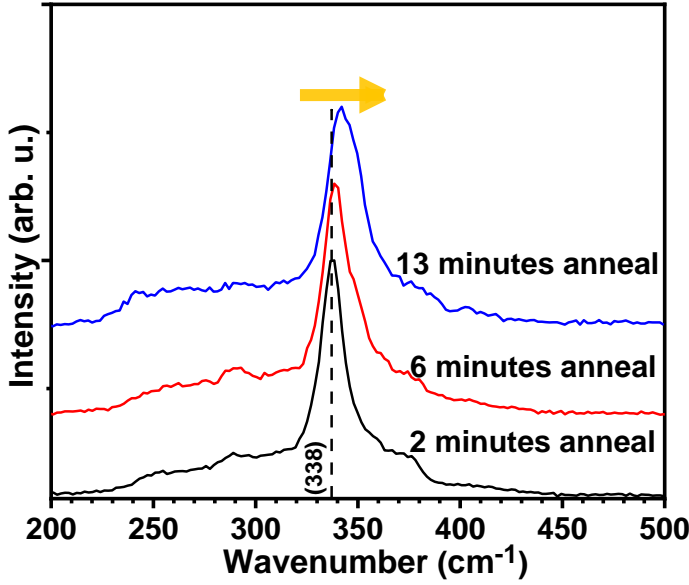


Figure 18 Raman shift of sulfurized CZTS/CZGS absorbers with the increase in annealing duration. The data is adapted from Paper-II [34].

The formation of a compositional gradient occurred with the competing mechanism of Ge diffusion through grain boundaries, leading to a few Ge-rich nano-regions on the surface of the bilayer (see Figure 19). This can be seen clearly in STEM/EDS, which showed the detailed compositional mapping of the complete thin film at different anneal durations. Ge and Sn intermixed differently because Sn diffused into the grain interior, whereas Ge diffused across grain borders. The resulting compositionally graded film does not contain smooth compositional grading as opposed to what is indicated from GDOES measurement of the compositionally graded films. Instead, a steep gradient existed with the combination of Ge-or Sn-rich grains, graded grains, and the presence of Ge around the grain boundaries (Paper-II).

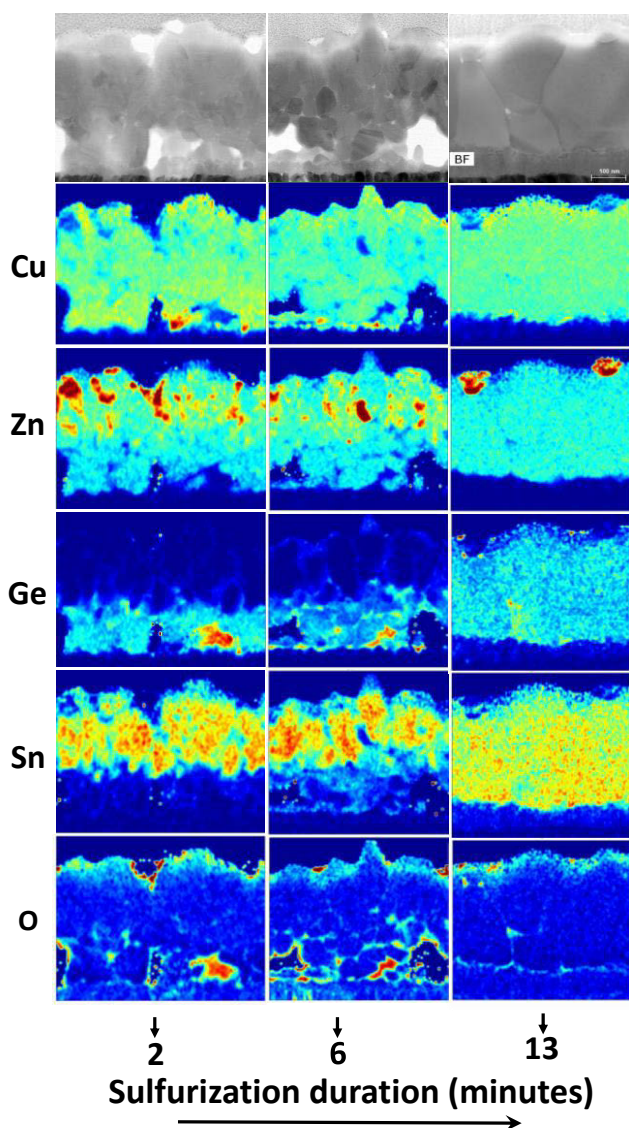


Figure 19 STEM/EDS images of sulfurized bilayered absorber for a different duration. The data is taken from Paper-II [34]. The secondary phases such as ZnS, Cu_xS , GeO_x can be confirmed here, which is also consistent with Raman spectra (for ZnS in Paper-II), XRD spectra (for ZnS in CZGS Paper-IV), and XPS spectra (for GeO_x in Paper-IV)

In paper-III, CZTS/CZGS bilayers were fabricated with an interlayer (TiN) beneath them. Thick CZTS layers (600, 800, and 990 nm) were sputter-deposited on thin CZGS films of different thicknesses (100 nm and 200 nm) to fabricate CZTS/CZGS structure. CZGS films were air-exposed since the composition of CZGS was needed to be measured before deposition of CZTS.

So, a series of six samples were sulfurized under different sulfurization conditions with varying sulfurization duration of 1, 6, and 8 minutes without changing other sulfurization conditions.

TiN interlayer can affect Na diffusion to the absorbers [57], and controlled addition of Na in the absorber can improve the grain growth [134]. In addition, grain growth can be improved with a low concentration of Germanium, as described earlier. Atomic diffusion occurs faster through grain boundaries than grains [135]. Therefore, unlike graded absorbers (Paper-II) with Mo-coated glass substrates, the CZTS/CZGS absorbers show a slight $[\text{Ge}]/([\text{Sn}]+[\text{Ge}])$ gradient when fabricated on TiN/Mo/SLG (Paper-III). The few differences between both investigations (paper-II and Paper-III) are the thicknesses of both layers (CZGS and CZTS), sodium GDOES profiles, and reduced anneal duration. This can affect Ge interdiffusion by accelerating the movement of atoms across grain boundaries. In general, low Ge concentration (thin CZGS underneath CZTS) and the formation of slightly bigger grains in the absorbers are linked with the disappearance of Ge-Sn gradients.

5.3 CZGTS solar cell devices

CZGTS solar cell devices were fabricated using a similar structure as for CZTS solar cells. The devices could be optimized for each layer from back contact to front contacts. In this section, some issues such as delamination, back contact, and buffer layers are discussed.

5.3.1 Delamination and insertion of an adhesive TiN interlayer

Secondary phases and defects strongly control the performance of chalcogenide solar cells [60,108,134,136,137]. The secondary phases can cause a slight change in the bulk composition of the absorbers. Cu-rich and Zn-rich sides of the CZTS could not exceed than stoichiometric CZTS [138]. In addition, sulfur incorporation and reaction to Mo could lead to secondary phases [105,139]. The formation of insulating (ZnS , GeO_x) [60,140] or highly conductive (Cu_xS) phases in bulk or interfaces could be detrimental to the device performance. Therefore, etching is required to remove the secondary phases from the surface of the absorber. KCN-etching was used repeatedly on CZGTS absorbers, but it sometimes resulted in delamination of the complete film. In these experiments, the loss of adhesion between multilayers can occur due to many reasons such as reduction of adhesive contacts, mismatched thermal expansion, extreme interfacial stress or strains, and formation of water-soluble phases (GeO_x) [141,142]. The formation of GeO_x layer could be confirmed in STEM/EDS mapping of the CZGTS films (Paper-II, Paper-III, Paper-IV). The GeO_x phase was mostly present on the grain boundaries and

voids of the thin film. In addition to this, adhesion can change with the formation of the MoS₂ layer. Therefore, a series of CZGS precursor was co-sputter deposited at different temperatures (200 °C, 250 °C, and 300°C) and sulfurized with different conditions (temperature = 560, 580, 600°C, time = 1, 6, 13 minutes). CZGTS absorbers typically adhere to the addition of a TiN inter-layer between Mo and CZGS irrespective of change in deposition or annealing condition. So, the CZTS/CZGS solar cells were prepared with TiN/Mo/SLG in Paper-II. However, as shown in Paper-II, the TiN layer does not completely resolve the delamination issue as it still persists in some solar cells.

5.3.2 CZTS/CZGS solar cell devices

CZTS/CZGS absorbers were prepared on TiN/Mo/SLG substrates for all solar cells. In Paper-III, different layers with varying thicknesses of CZGS (100 and 200 nm) and CZTS (600, 800, 990 nm) were deposited with a similar structure as defined for CZTS/CZGS absorbers. While the aim was to form a Ge-Sn gradient after annealing of the stack, most of the samples showed close to uniform composition as already described. The samples are named as given in Table 3.

Table 3 Naming of the different CZTS/CZGS precursors with approximate GGS [Ge]/([Sn]+[Ge]) ratio in Paper-III. The average composition of the individual layer was measured by XRF calibrated with RBS.

Film type – thickness, composition	CZTS - 600 nm Cu/Sn = 1.86 ± 0.01, Zn/(Cu+Sn) = 0.36 ± 0.002	CZTS - 800 nm Cu/Sn = 1.89 ± 0.008, Zn/(Cu+Sn) = 0.36 ± 0.001	CZTS - 990 nm Cu/Sn = 1.87 ± 0.008, Zn/(Cu+Sn) = 0.36 ± 0.002
CZGS - 100 nm Cu/Ge = 1.84 ± 0.05, Zn/(Cu+Ge) = 0.35 ± 0.003	10Ge60 GGS = 0.14	10Ge80 GGS = 0.11	10Ge99 GGS = 0.09
CZGS - 200 nm Cu/Ge = 1.85 ± 0.04, Zn/(Cu+Ge) = 0.36 ± 0.002	20Ge60 GGS = 0.25	20Ge80 GGS = 0.2	20Ge99 GGS = 0.17

In this series, the overall Ge content of the samples varies due to different thicknesses of the CZGS and CZTS thin films. A few solar cell absorbers peeled off during KCN etching, and solar cells were not fabricated for those samples. The performance of the CZTS/CZGS solar cells did not improve compared to CZTS reference solar cells (see Table 4). J-V characterization of a solar cell fabricated from one minute anneal of 20Ge99 showed a rollover behavior (see Figure 20). For the same sulfurization duration, a higher J_{sc} was

measured for 20Ge60 compared to 20Ge99. However, the estimated current density obtained from EQE was higher for 20Ge99 than for 20Ge60.

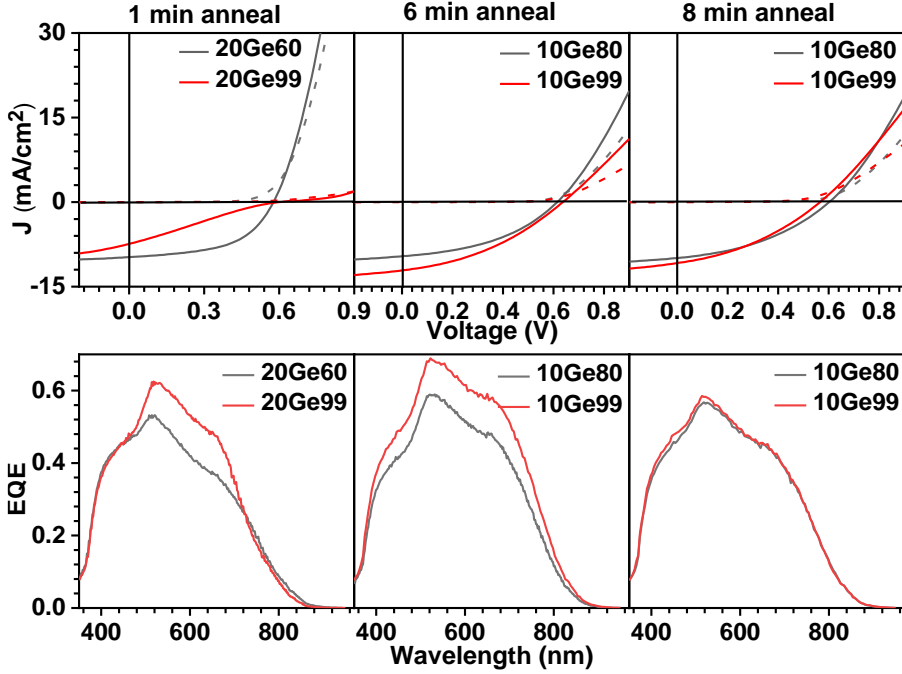


Figure 20 J-V and EQE characteristics of CZTS/CZGS bilayers annealed for 1 min, 6min, and 8 minutes. The figure is adapted from [143].

This behavior could be partly related to series resistance or different illumination intensity and spectra between J-V and EQE measurement. EQE measurement was done under low illumination of monochromatic light.

The band gap change with the incorporation of Ge can be verified with a change in the long-wavelength edge in EQE. J-V curves of all the bilayer devices showed a cross-over (non-ideal diode) behavior between dark and illuminated curves. The rollover behavior could happen due to poor pn-junction quality, poor band alignment, and insulating secondary phases on the front or back interface. An s-shaped J-V curve of the bilayer solar cell could possibly originate from the increased degree of order and a hole barrier at the back interface [144]. Additionally, the expected cliff-like band alignment at the front interface of CZGTS due to the upshift of the conduction band would enhance recombination [19]. So, the interface recombination could be expected to increase in CZGTS solar cell devices as compared to CZTS.

Table 4 Solar cell parameters of best solar cell devices fabricated from annealed bi-layer CZTS/CZGS. Note that the delaminated solar cells are not included in this table. Please refer to Paper-III [143] for more details.

Sulfurization batch	Name	GGS	V_{oc} (V)	J_{sc} (mA/cm ²)	FF (%)	η (%)	J_{sc} (mA/cm ²) (EQE)
One minute sulfurization	20Ge6 ₀	0.25	0.576	9.8	53	3.0	10.1
	20Ge9 ₉	0.17	0.603	7.4	23	1.0	11.4
	CZTS-60	0	0.641	12.0	55	4.2	13.6
	CZTS-99	0	0.652	7.5	51	2.5	11.1
Six minutes sulfurization	10Ge8 ₀	0.11	0.614	9.6	42	2.5	11.7
	10Ge9 ₉	0.09	0.637	12.1	37	2.9	14.1
	CZTS-80	0	0.621	13.8	51	4.4	14.4
	CZTS-99	0	0.473	10.2	39	1.9	11.6
Eight minutes sulfurization	10Ge8 ₀	0.11	0.608	11.0	42	3.0	11.5
	10Ge9 ₉	0.09	0.596	11.7	43	3.0	11.7
	CZTS-80	0	0.601	13.1	50	4.0	14.0
	CZTS-99	0	0.596	14.9	45	4.0	15.2

5.4 Alternative ZTO buffer for CZGS

In this series, the investigations were done to focus mainly on two issues. 1) the cliff-like band alignment between CZGS absorbers and CdS, and 2) the delamination of CZGS absorbers in aqueous KCN or water.

Therefore, complete dry processing of CZGS absorbers was used to fabricate solar cells. ZTO buffer layers were chosen since the band gap of these layers can be changed with a change in deposition condition. Although ZTO should form a cliff-like band alignment with the CZGS absorber, the effect of band alignment change can still be investigated.

In Paper-IV, alternative buffer layers on CZGS absorbers were investigated (See Table 5) to reduce the front interface recombination that was pointed out

as a possible issue in the CZGTS devices in Paper-III. The effect of etching of the absorbers was investigated. Etching of the absorbers could remove insulating phases such as GeO_x in Paper-IV, leading to improved J_{sc} than non-etched CZGS solar cells. This study compares the performance of solar cells produced using etched CZGS with CdS and ZTO buffer layers. FF decreased with the usage of the ZTO layer. High current density and V_{oc} could be measured by ZTO buffer layer deposition along with a large spread. Such a large spread in device parameters can occur due to partial delamination during KCN etching of the absorbers. Therefore, ZTO layers were deposited on unetched CZGS absorbers at different deposition temperatures. CZGS solar cell performance was observed to be insensitive to ZTO deposition temperature and thickness. The band alignment and composition of ZTO could be tuned with deposition temperature; however, the V_{oc} of the non-etched devices was relatively constant. This could likely be due to an oxide interlayer remaining between CZGS and ZTO. The solar cell performance of CZGS fabricated with ZTO buffer layer showed V_{oc} over 1 V but with a lower current density than expected due to insulating phases on the front interface (Table 5).

Table 5 ALD deposition conditions for different ZTO buffer layers and solar cell parameters obtained from different CZGS of comparable composition. Note that CZGS absorbers were fabricated from different batches (A and B). CZGS of similar compositions were used. This table is adapted from Paper-IV.

Sample name	ALD deposition conditions		Solar cell parameters			
	Temperature (°C)	No. of ALD cycles	J_{sc} (mA/cm ²)	V_{oc} (V)	FF (%)	η (%)
A1	90	1000	2	0.963	36	0.7
A2		750	1.8	0.842	38	0.6
A3		1000	2.1	1.1	38	0.85
A4	100	750	2.2	0.957	36	0.76
A5		500	2.4	0.974	36	0.85
A6		1000	3.2	0.917	45	1.3
A7	110	750	2.2	0.854	43	0.8
A8		500	2.1	0.88	35	0.7
B1		1000	2	0.931	45	0.85
B2	120	750	2	0.989	40	0.8
B3		500	1.9	0.819	40	0.6

5.5 Ultrathin CZTS with passivation layer

Ultrathin CZTS layers could be an essential material for multijunction solar cells as mentioned in chapter 2. In this thesis, CZTS of approximately 300 nm thickness was utilized for tandem solar cell fabrication based on optimized optical simulation to match photocurrent [145].

An experimental series was made where backside passivation layers such as Al_xO_y , SiO_x were deposited on back-contact Mo. The thickness of Al_xO_y and SiO_x was estimated to be close to 1 nm for the thinnest layers, and thickness up to ≈ 10 nm was used. In literature, ultrathin Al_2O_3 [146–148] have been reported to show passivation of the absorbers. The explanation for passivation from such thin layers could be that the first few nanometres of Al_2O_3 layer [147–152] might be associated with a high density of negative charges [148,151] in addition to the controlled reaction on back-contact [153]. Similar layers such as TiN and polySi can be used as protection layers for Si tandem solar cells (not shown here). The presence of the oxide layers could be confirmed by XPS (not shown here). Al_xO_y was deposited by reactive sputtering as well as ALD. Ultrathin CZTS (≈ 300 nm) absorbers was prepared by co-sputtering and sulfurization. Solar cells were completed by deposition of CdS, i-ZnO, and AZO layers (See Figure 21). CZTS recrystallized with similar grain (≈ 300 nm) growth. Absorbers were detached from sputter-deposited Al_xO_y (≈ 1 nm). The thickness of MoS_2 was seen to be slightly decreased.

SiO_x and Al_xO_y [154] showed passivation, irrespective of different deposition methods such as plasma-assisted or thermal ALD [155–157], Plasma enhanced chemical vapor deposition (PECVD) [157], and high throughput industrial sputter deposition [153]. An ultrathin passivation layer or a passivation layer with nanosized point contacts can limit the Mo/CZTS contact region, reducing the negative impact of SnS and ZnS secondary phases [58,158,159].

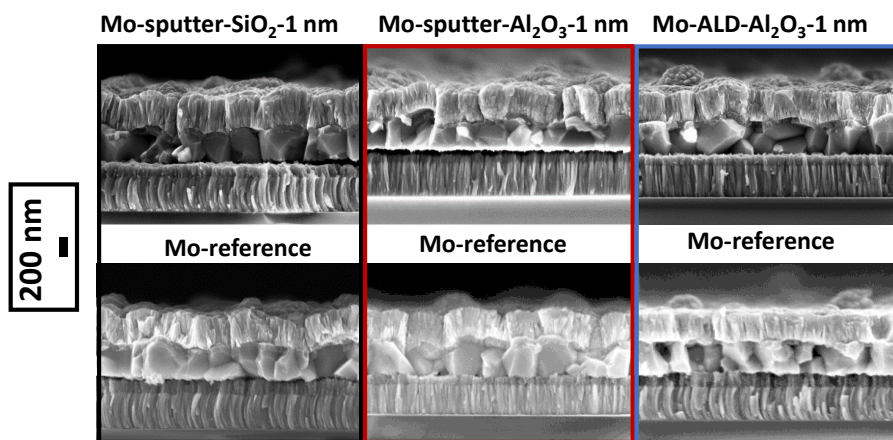


Figure 21 Cross-section SEM image of the backside passivated solar cell along with their reference solar cells. Ultrathin CZTS delaminated when deposited on sputter-deposited Al_xO_y as seen in the back-interface cross-section image.

Solar cell characterization of passivated and Mo-reference solar cell are shown in Figure 22. The overall performance of the solar cell improved with

1 nm passivation layer (sputter SiO_x and ALD Al_xO_y) as shown by J-V characterization. The improved J_{sc} was confirmed by EQE. Solar cells with sputtered 1 nm Al_xO_y showed blocked behavior. Photoluminescence spectra of the absorbers with buffer layer was improved in all the cases. Solar cells with thick passivation layers showed blocked behavior with the issue of delamination (not shown here). Thus, ultrathin passivation layers did not deteriorate conduction in solar cells. Highest 6.15 percent efficient ultrathin kesterite CZTS thin-film solar cell ($V_{oc} = 598 \text{ mV}$, $J_{sc} = 16.5 \text{ mA/cm}^2$, $\text{FF} = 62.2 \%$) is achieved with an ultrathin passivation layer.

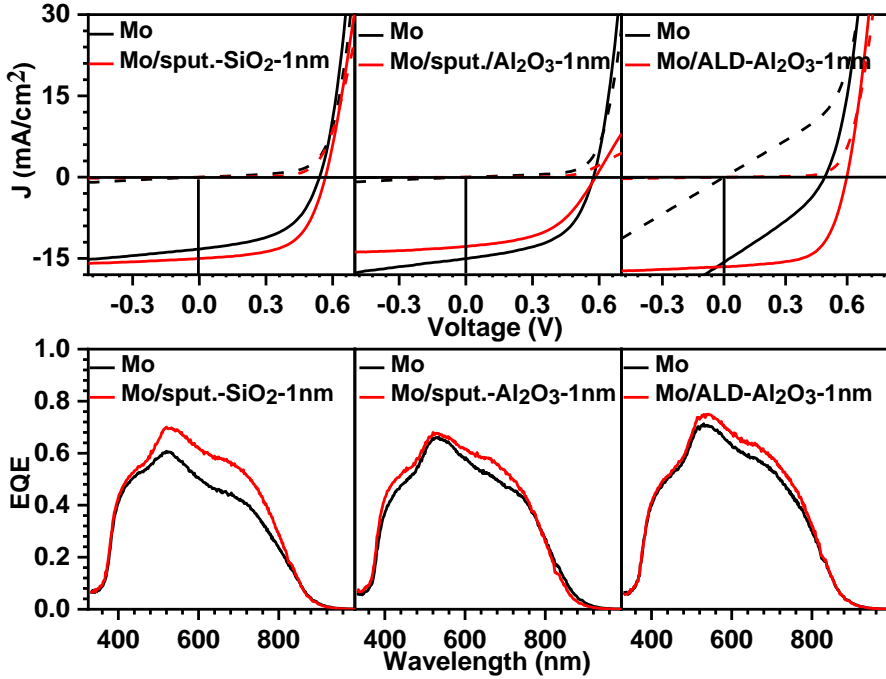


Figure 22 J-V and EQE characteristics of ultrathin CZTS solar cells deposited with backside passivation layer of Silica and Alumina. Al_xO_y layer was also deposited by sputtering and ALD. Each solar cell characteristic curve is plotted with its reference CZTS solar cell. J_{sc} and V_{oc} of the passivated solar cell improved except for sputtered Al_xO_y primarily owing to poor back-interface. Thickening of the sputter-deposited Al_xO_y layer led to complete delamination of CZTS.

Ultrathin CZTS was also applied to TOPCon Si-tandem solar cells in collaboration with DTU. The optimized thickness of CZTS had been reported about 300 nm by optical simulations and matched photocurrent density of single junction CZTS solar cell [91,145]. Initial tandem solar cell efficiency was 6.8 % ($V_{oc} = 1083 \text{ mV}$, $J_{sc} = 10.8 \text{ mA/cm}^2$, $\text{FF} = 58.6 \%$), but there is large room for optimization of several processing steps (not shown here). Also, other impurities such as sodium might affect the CZTS properties, but this was not investigated in tandem solar cell structure. Cu contamination of bulk Si

was not affected by varying sulfurization duration during the fabrication of thin CZTS. The diffusion of Cu atoms from CZTS to bulk-Si was mainly reduced by using multilayer diffusion barrier of $\text{SiO}_x(1.2 \text{ nm})/\text{polySi}(200 \text{ nm})/\text{TiN}(2.5 \text{ or } 5 \text{ nm})$ to improve charge carrier lifetime in bulk Si.

6 Summary of conclusions and outlook

6.1 Conclusion

The aim of this thesis was to investigate the incorporation of Ge into CZTS to reduce bulk and interface losses. A two-step fabrication process involving sputtering of stacked compound layers and annealing in the sulfur atmosphere was used. The goal was to fabricate compositionally graded CZGTS absorber films for band gap engineering in solar cells and to investigate the influence of Ge alloying in CZTS on material properties. A germanium-rich CZGTS layer on the backside can provide an upshift in the conduction band to repel electrons from the back surface to reduce interface recombination. Ultrathin CZTS solar cell absorbers with oxide passivation layers on the backside were also investigated as an alternative to back grading for very thin CZTS. Additionally, CZGS solar cells with different buffer layers were deposited to investigate improvements at the front interface from improved conduction band alignment between the absorber and buffer layers.

In paper-II, it was shown that synthesis of CZGS under sulfur-rich sputter conditions led to wurtzite-like phases of CZGS. Once the mixture was formed, it could not be transformed to kesterite phase by annealing ($\approx 582^\circ\text{C}$). It was seen that sulfurization of CZTS with a low concentration of Ge led to improved grain growth compared to a high concentration of homogenous CZGTS alloy. Additionally, a steep band gap grading was achieved using sulfurization of CZTS/CZGS films. The steep grading between larger Sn-rich grains at the front and smaller Ge-rich grains at the back was confirmed by STEM/EDS in contrast to smooth compositional grading seen with GDOES in the same sample. So, detailed information is always needed to quantify compositional grading.

The graded absorbers and sulfurized CZGS were delaminated with KCN etching. Therefore, the introduction of an adhesive TiN layer between Mo and CZGTS was investigated in paper III. TiN improved the adhesion markedly, but some delamination issues remained that influenced the studies in paper III and IV.

STEM/EDS showed oxygen-rich grain boundaries and voids with Ge-rich samples, and surface oxides, most likely GeO_x , were removed from CZGTS in etching. Since this oxide is water-soluble, there is a possible connection to the delamination issues for Ge-containing films.

A mild compositional gradient was observed on TiN substrate in contrast to a previous study (Paper-II). The composition gradient depends on atomic diffusion through grains and grain boundaries, which depend on recrystallization. A small concentration of Ge and Na could affect the recrystallization process. Since the Ge increased at the front of the film, it is possible that a beneficial effect of Germanium in bulk or towards the back contact could be negated by an increasing cliff-like band alignment with the CdS buffer.

If recombination at the back contact is limiting solar cell performance, passivation of this interface can improve performance. Passivation aims at reduced recombination and can be achieved by so-called chemical passivation where the density of recombination states is reduced, or field-effect passivation, where the availability of charge carriers that can contribute to the recombination current, in this case, electrons, is reduced. Band gap grading towards the back contact is one way that also extends into the bulk, and the introduction of a blocking layer, often an oxide, is another. In this thesis, Al_xO_y and SiO_x were investigated as passivation layers for ultrathin (≈ 330 nm) CZTS.

A thick oxide passivation layer can provide the passivation effect but with the loss of conductivity. So, very thin (≈ 1 to 2 nm) Al_xO_y and SiO_x layers were deposited on Mo/SLG. The solar cell parameters improved with insertion of a very thin oxide layer; however, blocking behavior was observed with increased thickness of passivation layer. From photoluminescence, the improvement was seen only for the thinnest oxide passivation layer. The optoelectronic parameters (V_{oc} , J_{sc} , and FF) of the solar cell improved with the thinnest passivation layer compared to non-passivated solar cells. Furthermore, the ultrathin CZTS solar cells were monolithically integrated with crystalline Si solar cells using a diffusion barrier of p^+ polycrystalline-Si/ SiO_x /TiN layers. The variation in sulfurization duration of CZTS did not change diffusion of Cu with the presence of diffusion barrier on Si solar cell.

A wide band gap ZTO layer constituting non-toxic, earth-abundant elements could be an alternative to CdS buffer. In order to avoid delamination, complete processing of the non-etched CZGS with ZTO (CZGS/ZTO) buffer layers was investigated (Paper-IV). Several ZTO buffer layers of varying thicknesses were deposited at different deposition temperatures. Similar V_{oc} of CZGS/ZTO solar cells were observed, in contrast to the expected variation with changing buffer layer band gap. The V_{oc} was relatively high, up to 1.1 V for CZGS/ZTO solar cells, which was substantially higher than for CZGS/CdS. Another comparison of CZGS/ZTO solar cells was made with etched and non-etched CZGS absorbers. The short-circuit current of the solar cells improved with etching which could probably be related to the removal of GeO_x . A blocking oxide interlayer is also a possible explanation for the small variation in V_{oc} for non-etched devices. The solar cells with etched absorbers showed a large spread in solar cell parameters.

6.2 Future work

Based on the aforementioned conclusion, further investigations are proposed in the following areas:

1. An investigation is required on Ge incorporated CZTS to find a root cause of delamination. Water-soluble phases such as GeO_x could be found on the surface, grain boundaries, and voids of the absorber. So, an annealing series with different air-exposure time can be investigated.
2. The etching of the GeO_x layer from the interface could be instrumental for improved solar cell performance. So, dry etching of secondary phases can be very useful.
3. Cation order-disorder of CZGS or CZGTS can be investigated. The origin of photoluminescence emission peaks at lower energy could be investigated.
4. Alternative wide band gap buffer layers such as $\text{Zn}_{1-x}\text{Ge}_x\text{O}_y$, $\text{Sn}_x\text{Ge}_{1-x}\text{O}_y$, ZnS , and $\text{Zn}(\text{O},\text{S})$ etc. should be investigated with CZGS or graded absorbers.
5. Back-surface passivation of the ultrathin CZTS should be investigated with transparent back contact. The passivation layer can control the overall back-interface recombination due to improved interface.

In general, CZGTS absorbers can show improved performance at a low concentration of Ge. Front interface improvement and etching of residual secondary phases from the absorber can benefit device performance. Additionally, understanding the material properties of CZGTS can provide important information about the origin of defect states.

7 Svensk sammanfattning

Tunnfilmssolceller har många användningsområden som bygger på egenskaperna hos de använda materialen. Några av de fördelar som finns hos tunnfilms-solceller i jämförelse med kristallina kisel-solceller är reducerad materialåtgång, möjligheten att variera band gapet, flexibilitet, låg energiåtgång vid tillverkning, låg vikt vid deponering på lätta substrat samt estetiskt utseende. Det finns några olika framgångsrika tunnfilmsteknologier som $\text{Cu}(\text{In,Ga})\text{Se}_2$ (CIGS) och CdTe som finns kommersiellt, men marknadsandelen i förhållande till kisel sjunker för närvarande av olika skäl. Det främsta är utmaningen att hålla jämna steg med den kontinuerliga kostnadsreduktionen i kiselteknologin, med betydligt större tillverkningsvolym. En annan fråga som länge uppmärksammats är användningen av grundämnen som indium och tellurium som är mindre vanligt förekommande än kisel. Alternativa material som bara innehåller väldigt vanliga grundämnen har därför undersökts, som $\text{Cu}_2\text{ZnSn}(\text{S,Se})_4$ (CZTSSe). Verkningsgraden för solceller av CZTSSe ökade snabbt men har sedan planat ut, och orsaken är troligen defekter i materialet som är svåra att undvika. För filmer utan selen, dvs CZTS, är prestandan ytterligare något lägre än teoretiskt möjligt. The skadliga defekterna har rapporterats vara Sn-relaterade, djupa defekter. Utbyte av Sn med Ge höjer band gapsenergin och kan kanske också minska de djupa defekterna. Tidigare studier av tillsats av Ge har visat positiva effekter på solceller med selen, CZTSSe. Studier av legering med Ge i den rena sulfiden CZTS, vilket är fokus i denna avhandling, är mindre vanliga.

Syftet med denna avhandling är därför att studera inblandning av Ge i CZTS för att minska förluster i bulken och vid gränsyterna. En tvåstegsprocess med deponering av sulfidfilmer genom sputtring har använts, följt av värmebehandling i svavelatmosfär. Målet var att tillverka CZGTS-filmer med en sammansättningsgradient i djupled för band gapsstyrning i solcellerna och att undersöka inverkan av legering med Ge i CZTS på materialegenskaperna. Ett germaniumrikt lager mot bakkontakten kan skifta ledningsbandskanten mot högre energinivåer, vilket minskar rekombinationsförlusterna. Passiveringslager av oxidmaterial vid bakkontakten undersöktes också som alternativ till band gapsgradering för väldigt tunn CZTS. Dessutom undersöktes CZGS-solceller med olika buffertlager som deponerats för att undersöka om en höjning av ledningsbandskanten i gränsytan mot absorbatoren kan minska förlusterna vid den gränsytan.

I paper II visades att tillverkning av CZGS under svavelrika deponeringsförhållanden ledde till wurtzit-fas efter sputtring. När väl denna fas bildats försvårades kristalliseringen till den önskade kesteritfasen under värmebehandlingen. För filmer med varierade mängd Ge sågs ökad korntillväxt för låga halter Ge. Genom värmebehandling av filmer där CZTS deponerats ovanpå en CZGS-film kunde CZGTS med sammansättningsgradient skapas. En skarp gradient sågs med mikroskopi, medan profilering med så kallad GDOES påvisade svaga Sn-Ge gradienter. Orsaken var en ojämn fördelning med i huvudsak stora Sn-rika korn på framsidan och mindre Ge-rika korn på baksidan vilket i medeltal över större yta gav en svag gradient. Detta visar på vikten av att använda kompletterande analys, särskilt mikroskopi med hög upplösning.

De värmebehandlade filmerna delaminerade vid den våtkemiska ets som vanligen används vid solcellstillverkningen. Därför undersöktes TiN som vidhäftningsskikt mellan Mo och CZGS i paper III. TiN ökade vidhäftningen markant, men viss delaminering förekom fortfarande vilket påverkade studierna både i paper III och IV. För filmer innehållande Ge sågs syre i korngränser och håligheter med STEM/EDS. På ytan av CZGTS sågs germaniumoxid som försvann vid våtkemisk etsning. Eftersom denna oxid också är vattenlöslig finns en möjlig koppling till vidhäftningsproblemen för Ge-innehållande filmer.

En svag Sn-Ge gradient erhöles i paper III, och utjämningen av gradienten under värmebehandling skedde något snabbare än för filmerna i paper II. Skillnaden mellan de båda studierna är användningen av TiN-skiktet vid bakkontakten, men olika tjocklekar användes också. Solceller med denna Ge-gradient hade lägre prestanda än referensceller av CZTS. Eftersom den erhållna Ge-gradienten också ökade Ge-halten på framsidan av absorbatoren, är det möjligt att en förbättring av egenskaper i bulken eller mot bakkontakten motverkades av ett sämre gränsskikt mot CdS bufferten.

Om rekombination vid bakkontakten begränsar solcellernas prestanda kan passivering av bakkontakten ge högre verkningsgrad. Passivering syftar till minskad rekombination vid bakkontakten och fås antingen genom sk kemisk passivering, där koncentrationen av energitillstånd som kan bidra till rekombination minskas, eller fält-effektpassivering, där tillgången på laddningsbärare som kan ge rekombinationsström minskas, i detta fall elektroner. Band gapsgradering mot bakkontakten är ett sätt, vilket också sträcker sig in i bulken, och introduktion av ett blockerade lager, ofta en oxid, ett annat. I denna avhandling undersöktes Al_2O_3 och SiO_2 som passiveringsskikt för ultratunn CZTS. Tjockleken på oxiden varierades från någon nanometer upp till ca 20 nm. För de tjockare oxiderna blockerades strömmen som väntat och för den tunnaste oxiden sågs en svag förbättring. Med fotoluminiscens sågs också svag förbättring för den tunnaste oxiden men inte för tjockare oxider. Fortsatta studier av mönstrade oxider som inte blockerar strömmen vore intressant liksom bättre förståelse av förbättringen för den tunnaste oxiden.

Ett alternativt buffertlager för CdS, med högt band gap och utan giftiga ämnen, är $\text{Zn}_{1-x}\text{Sn}_x\text{O}_y$ (ZTO), tillverkad med ALD. I paper IV studerades detta material för solceller av CZGS. På grund av problem med delaminering, trots användning av TiN, gjordes huvuddelen av solcellerna utan våtkemisk etsning. För dessa sågs höga spänningsnivåer, upp till 1.1 V, men inverkan av deponeringstemperatur var oväntat svag och strömmen mycket låg. En jämförelse mellan CZGS/ZTO med och utan ets visade en fördubbling av strömmen. En möjlig förklaring till dessa båda resultat är ett blockerande gränsskiktsslag, troligen germaniumoxid. En jämförelse mellan CZGS/CdS och CZGS/ZTO med ets i båda fallen visade högre spänning för ZTO, men ledningsbandskanten för ZTO är troligen lägre än optimalt, även om den är högre än för CdS. Fortsatta studier av ZTO för CZGTS med lägre band gap än CZGS är därför mycket lovande medan andra buffertmaterial med ännu högre band gap bör undersökas för ren CZGS.

8 Acknowledgments

Pursuing a Ph.D. has been a great learning experience as it has allowed me to explore solar cell research and improve my self-perception. I am immensely thankful to many people since it would not have been possible to finish this thesis without their support and assistance.

First and foremost, I would like to thank **Charlotte**, my principal supervisor, for accepting me as your Ph.D. student and showing faith in my abilities. Thank you so much for all the ideas, explanations, criticism, discussion, encouragement, patience, and continuous support from beginning to the end of my Ph.D. Your unparalleled positive attitude, energy, and enthusiasm have helped to refine my work. You are an incredible role model for my future career. Thanks, **Ingrid**, for the administrative work and continuous help with resident permit issues. The initial period of my Ph.D. was quite difficult for me, and both of you have been immensely helpful whenever I need your help. Thanks, **Svante**, for helping in finding an apartment before my arrival and all your technical support in solar cell measurement laboratory.

I owe a significant portion of my acknowledgment to **Jes**, my co-supervisor, for being very kind, sharing his critical feedback, and finding time for numerous discussions on research work. Thanks for introducing me to various tools in the lab and your valuable input to this thesis. My deepest gratitude to **Jonathan S** for providing critical feedback on thesis preparation, open discussion on new ideas, and significant help troubleshooting SUSE. **Katharina**, I appreciate your kind chats and much help in the laboratory. Thank you, **Sven**, for tasty solar cell cake, interesting Swedish stories, accepting my invitation to India, gifting plants, and introducing me to ping-pong. Thanks to **Nils** for training me on the various lab protocols and continuous support for BEA. Thanks to former colleagues: **Christopher**, **Yi R**, **Tove**, **Volodymyr**, and **Alexandra** for their valuable contributions to the group. **Corrado** and **Patrick**, all the best and have a lot of fun in the remaining time of your Ph.D.

Marika, thanks for a positive outlook, inspiration, taking care of the group, and smoothly running the whole division. Thanks to **Faraz** for regular coffee breaks, research work, fun chat, support, and sharing the whole Ph.D. time with me. I wish you a good luck for the rest of your Ph.D. work. Thanks to **Jan**, **Wei-Chao**, and **Rongzhen** for sharing your critical queries on my research and positive spirit. **Kostya** for introducing a vegan person to fishing ;),

berry/mushroom picking, being always critical, and supportive. Thanks to **Uwe** and **Adam** for your continuous support in the measurement lab, cleanroom, and keeping the Friday beer legacy alive. I occasionally thought that without you and **Jes**, the solar cell lab might cease to function. Thank you, **Tobias** and **Natalia**, for sharing your extensive expertise on ALD, XRD, and XPS. I appreciate **Lars S** and **Olof** for their support in the cleanroom and sharing their experience in the group meetings. I am grateful to **Carl**, **Bjorn L**, **Olivier**, and **Jörgen** for always being welcoming and helping. Thanks to the former solar cell group members **Sethu**, **Oleksandr**, **Fredrik L**, and **Dorothea** for always being very kind. I appreciate the whole solar cell technology division for having me as a part of the family. **Michelle**, **Nina**, and **Nagn** for kind chats. **Melike**, all the best for your future endeavors in the group. I hope that I shall again get a chance to work with many out of you in the future.

Thanks to **Tomas K** and **Tomas N** for their assistance and exciting chats on sputtering. I am also grateful to **Amit** for always helping in troubleshooting the sputter systems, BAK, and friendly chats. Thanks to **Farhad**, **Victoria**, **Örjan**, and **Rimantus** for smooth cleanroom operations. Thanks to **Ali-reza**, **Elizabeth**, **Sigbjørn**, **Kristina**, **Andrea**, **Hisham**, and **Lars R** for nice collaborations. Special thanks to my colleagues from the old division: **Shi-Li**, **Apurba**, **Siddharth**, **Robin**, **Ida A**, **Jacob**, **Syaiful**, **Mauricio**, **Dragos**, **Long**, **Imran**, **Renbin**, **Chenyu**, **Shuangshuang**, **Xingxing**, **Si**, and **Shiyu**. Thanks to **Lukas** and **Malkolm** for a short but fun time. I hope to have the opportunity to work with many of you again in the future.

Thanks to **Jonatan B**, for always resolving my computer problems. I am also grateful to **Ramy**, **Ida**, and **Maria S** for administration-related work.

Grateful to be a member of a champion beach volleyball team ;): **Jithin**, **Akshay**, **Rahul**, **Shibu**, **Sohan**, **Federico**, and **Sumalata**. I am thankful to my Indian friends **Vivek**, **Ritwik**, **Sangeeta**, **Devendra**, **Deep**, **Pritam**, **Suman**, **Deobrat**, and **Nisha** for sharing delicious Indian meals and their recipes with me. I am also thankful to my old friends **Abhay S**, **Lalit**, and a slew of others.

Last but not least; I want to express my sincerest gratitude to my family and parents in law. My mom for always loving me, and dad for always teaching the important life lessons, my brother for cherishing enjoyable moments with me, and my wife for unequivocal support throughout the Ph.D. journey.

I could go on indefinitely to acknowledge every person in my life since everyone has contributed directly or indirectly to my accomplishments, and Ph.D. is not an isolated event of my life, but there would never be enough space to do so. I am forever grateful to all.

9 References

- [1] J. Rowlatt, L. Knight, The real reason humans are the dominant species, BBC News. (2021). <https://www.bbc.com/news/science-environment-56544239> (accessed August 26, 2021).
- [2] International Energy Agency, Global Energy Review 2019: The latest trends in energy and emissions in 2019, OECD, 2020. <https://doi.org/10.1787/90c8c125-en>.
- [3] T. Waterfield, In: Global Warming of 1.5°C. An IPCC Special Report on the impacts of global warming of 1.5°C above pre-industrial levels and related global greenhouse gas emission pathways, in the context of strengthening the global response to the threat of climate change, sustainable development, and efforts to eradicate poverty, World Meteorological Organization, Geneva, Switzerland, 2018. <https://www.ipcc.ch/sr15/> (accessed August 26, 2021).
- [4] W.F. Lamb, T. Wiedmann, J. Pongratz, R. Andrew, M. Crippa, J.G.J. Olivier, D. Wiedenhofer, G. Mattioli, A.A. Khourdajie, J. House, S. Pachauri, M. Figuerola, Y. Saheb, R. Slade, K. Hubacek, L. Sun, S.K. Ribeiro, S. Khennas, S. de la R. du Can, L. Chapungu, S.J. Davis, I. Bashmakov, H. Dai, S. Dhakal, X. Tan, Y. Geng, B. Gu, J. Minx, A review of trends and drivers of greenhouse gas emissions by sector from 1990 to 2018, *Environ. Res. Lett.* 16 (2021) 073005. <https://doi.org/10.1088/1748-9326/abee4e>.
- [5] B.F. Towler, Chapter 8 - Solar Power, in: B.F. Towler (Ed.), *The Future of Energy*, Academic Press, Boston, 2014; pp. 161–185. <https://doi.org/10.1016/B978-0-12-801027-3.00008-7>.
- [6] S. Weckend, A. Wade, G. Heath, End-of-life management: Solar Photovoltaic Panels, International Renewable Energy Agency, 2016. <https://www.irena.org/publications/2016/Jun/End-of-life-management-Solar-Photovoltaic-Panels> (accessed August 29, 2021).
- [7] E. Asmelash, G. Prakash, D. Gielen, R. Gorini, Future of solar photovoltaic, International Renewable Energy Agency, 2019. <https://www.irena.org/publications/2019/Nov/Future-of-Solar-Photovoltaic> (accessed August 29, 2021).
- [8] S. Connors, Frequently Asked Questions-IPCC — Intergovernmental Panel on Climate Change, IPCC, 2015. https://www.ipcc.ch/site/assets/uploads/sites/2/2018/12/SR15_FAQ_Low_Res.pdf (accessed September 18, 2021).

- [9] E. Hawkins, P. Ortega, E. Suckling, A. Schurer, G. Hegerl, P. Jones, M. Joshi, T.J. Osborn, V. Masson-Delmotte, J. Mignot, P. Thorne, G.J. van Oldenborgh, Estimating Changes in Global Temperature since the Preindustrial Period, *Bulletin of the American Meteorological Society*. 98 (2017) 1841–1856. <https://doi.org/10.1175/BAMS-D-16-0007.1>.
- [10] C.P. Morice, J.J. Kennedy, N.A. Rayner, P.D. Jones, Quantifying uncertainties in global and regional temperature change using an ensemble of observational estimates: The HadCRUT4 data set, *Journal of Geophysical Research: Atmospheres*. 117 (2012). <https://doi.org/10.1029/2011JD017187>.
- [11] Global and European temperatures — European Environment Agency, (2020). <https://www.eea.europa.eu/data-and-maps/indicators/global-and-european-temperature-10/assessment> (accessed September 17, 2021).
- [12] P. Breeze, Chapter 13 - Solar Power, in: P. Breeze (Ed.), *Power Generation Technologies* (Third Edition), Newnes, 2019: pp. 293–321. <https://doi.org/10.1016/B978-0-08-102631-1.00013-4>.
- [13] A. Aghahosseini, D. Bogdanov, C. Breyer, Towards sustainable development in the MENA region: Analysing the feasibility of a 100% renewable electricity system in 2030, *Energy Strategy Reviews*. 28 (2020) 100466. <https://doi.org/10.1016/j.esr.2020.100466>.
- [14] C. Breyer, D. Bogdanov, A. Aghahosseini, A. Gulagi, M. Child, A.S. Oyewo, J. Farfan, K. Sadovskaia, P. Vainikka, Solar photovoltaics demand for the global energy transition in the power sector, *Progress in Photovoltaics: Research and Applications*. 26 (2018) 505–523. <https://doi.org/10.1002/pip.2950>.
- [15] M. Victoria, N. Haegel, I.M. Peters, R. Sinton, A. Jäger-Waldau, C. del Cañizo, C. Breyer, M. Stocks, A. Blakers, I. Kaizuka, K. Komoto, A. Smets, Solar photovoltaics is ready to power a sustainable future, *Joule*. 5 (2021) 1041–1056. <https://doi.org/10.1016/j.joule.2021.03.005>.
- [16] Renewable Power Generation Costs in 2019, IRENA (2020), Abu Dhabi, 2020. <https://www.irena.org/publications/2020/Jun/Renewable-Power-Costs-in-2019> (accessed September 14, 2021).
- [17] M. Taylor, P. Ralon, S. Al-Zoghul, Renewable Power Generation Costs in 2019, International Renewable Energy Agency, 2020. <https://www.irena.org/publications/2020/Jun/Renewable-Power-Costs-in-2019> (accessed August 28, 2021).
- [18] C. Kost, S. Shammugam, V. Fluri, D. Peper, A.D. Memar, T. Schlegl, Study: Levelized Cost of Electricity - Renewable Energy Technologies - Fraunhofer ISE, Fraunhofer Institute for Solar Energy Systems ISE, 2021. <https://www.ise.fraunhofer.de/en/publications/studies/cost-of-electricity.html> (accessed August 30, 2021).

- [19] Q. Shu, J.-H. Yang, S. Chen, B. Huang, H. Xiang, X.-G. Gong, S.-H. Wei, $\text{Cu}_2\text{Zn}(\text{Sn},\text{Ge})\text{Se}_4$ and $\text{Cu}_2\text{Zn}(\text{Sn},\text{Si})\text{Se}_4$ alloys as photovoltaic materials: Structural and electronic properties, *Phys. Rev. B.* 87 (2013) 115208. <https://doi.org/10.1103/PhysRevB.87.115208>.
- [20] S. Chen, A. Walsh, Y. Luo, J.-H. Yang, X.G. Gong, S.-H. Wei, Wurtzite-derived polytypes of kesterite and stannite quaternary chalcogenide semiconductors, *Phys. Rev. B.* 82 (2010) 195203. <https://doi.org/10.1103/PhysRevB.82.195203>.
- [21] S. Chen, A. Walsh, X.-G. Gong, S.-H. Wei, Classification of Lattice Defects in the Kesterite $\text{Cu}_2\text{ZnSnS}_4$ and $\text{Cu}_2\text{ZnSnSe}_4$ Earth-Abundant Solar Cell Absorbers, *Advanced Materials.* 25 (2013) 1522–1539. <https://doi.org/10.1002/adma.201203146>.
- [22] S. Giraldo, M. Placidi, E. Saucedo, 5 - Kesterite: New Progress Toward Earth-Abundant Thin-Film Photovoltaic, in: D. Ginley, T. Fix (Eds.), *Advanced Micro- and Nanomaterials for Photovoltaics*, Elsevier, 2019: pp. 93–120. <https://doi.org/10.1016/B978-0-12-814501-2.00005-0>.
- [23] J. Andrade-Arvizu, R. Fonoll-Rubio, Y. Sánchez, I. Becerril-Romero, C. Malerba, M. Valentini, L. Calvo-Barrio, V. Izquierdo-Roca, M. Placidi, O. Vigil-Galán, A. Pérez-Rodríguez, E. Saucedo, Z. Jehl Li-Kao, Rear Band gap Grading Strategies on Sn–Ge-Alloyed Kesterite Solar Cells, *ACS Appl. Energy Mater.* 3 (2020) 10362–10375. <https://doi.org/10.1021/acsaem.0c01146>.
- [24] G.M. Ford, Q. Guo, R. Agrawal, H.W. Hillhouse, Earth Abundant Element $\text{Cu}_2\text{Zn}(\text{Sn}_{1-x}\text{Ge}_x)\text{S}_4$ Nanocrystals for Tunable Band Gap Solar Cells: 6.8% Efficient Device Fabrication, *Chem. Mater.* 23 (2011) 2626–2629. <https://doi.org/10.1021/cm2002836>.
- [25] S. Bag, O. Gunawan, T. Gokmen, Y. Zhu, D.B. Mitzi, Hydrazine-Processed Ge-Substituted CZTSe Solar Cells, *Chemistry of Materials.* 24 (2012) 4588–4593. <https://doi.org/10.1021/cm302881g>.
- [26] J. Chen, W. Li, C. Yan, S. Huang, X. Hao, Studies of compositional dependent $\text{Cu}_2\text{Zn}(\text{Ge}_x\text{Sn}_{1-x})\text{S}_4$ thin films prepared by sulfurizing sputtered metallic precursors, *Journal of Alloys and Compounds.* 621 (2015) 154–161. <https://doi.org/10.1016/j.jallcom.2014.09.097>.
- [27] E. Garcia-Llamas, M. Guc, I.V. Bodnar, X. Fontané, R. Caballero, J.M. Merino, M. León, V. Izquierdo-Roca, Multiwavelength excitation Raman scattering of $\text{Cu}_2\text{Sn}_{1-x}\text{Ge}_x(\text{S},\text{Se})_4$ single crystals for earth abundant photovoltaic applications, *Journal of Alloys and Compounds.* 692 (2017) 249–256. <https://doi.org/10.1016/j.jallcom.2016.09.035>.
- [28] G. Chen, W. Wang, S. Chen, Z. Whang, Z. Huang, B. Zhang, X. Kong, Bandgap engineering of $\text{Cu}_2\text{Zn}(\text{Sn}_{1-x}\text{Ge}_x)\text{S}(\text{e})_4$ by adjusting Sn-Ge ratios for almost full solar spectrum absorption, *Journal of Alloys and Compounds.* 718 (2017) 236–245. <https://doi.org/10.1016/j.jallcom.2017.05.150>.

- [29] L. Choubrac, G. Brammertz, N. Barreau, L. Arzel, S. Harel, M. Meuris, B. Vermang, 7.6% CZGSe Solar Cells Thanks to Optimized CdS Chemical Bath Deposition, *Physica Status Solidi (a)*. 215 (2018) 1800043. <https://doi.org/10.1002/pssa.201800043>.
- [30] D.B. Khadka, J. Kim, Band Gap Engineering of Alloyed $\text{Cu}_2\text{Zn}(\text{Ge}_x\text{Sn}_{1-x})\text{Q}_4$ (Q = S, Se) Films for Solar Cell, *The Journal of Physical Chemistry C*. 119 (2015) 1706–1713. <https://doi.org/10.1021/jp510877g>.
- [31] D.B. Khadka, J. Kim, Study of structural and optical properties of kesterite $\text{Cu}_2\text{ZnGeX}_4$ (X = S, Se) thin films synthesized by chemical spray pyrolysis, *CrystEngComm*. 15 (2013) 10500–10509. <https://doi.org/10.1039/C3CE41387J>.
- [32] C.W. Sinagra, F.O. Saouma, C.O. Otieno, S.H. Lapidus, J.-H. Zhang, A.J. Craig, P. Grima-Gallardo, J.A. Brant, K.A. Rosmus, K.E. Rossello, J.I. Jang, J.A. Aitken, Synthesis, structure, linear and nonlinear optical properties of noncentrosymmetric quaternary diamond-like semiconductors, $\text{Cu}_2\text{ZnGeSe}_4$ (CZGSe) and the novel $\text{Cu}_4\text{ZnGe}_2\text{Se}_7$, *Journal of Alloys and Compounds*. 888 (2021) 161499. <https://doi.org/10.1016/j.jallcom.2021.161499>.
- [33] L. Shi, P. Yin, H. Zhu, Q. Li, Synthesis and Photoelectric Properties of $\text{Cu}_2\text{ZnGeS}_4$ and $\text{Cu}_2\text{ZnGeSe}_4$ Single-Crystalline Nanowire Arrays, *Langmuir*. 29 (2013) 8713–8717. <https://doi.org/10.1021/la401531r>.
- [34] N. Saini, J.K. Larsen, K.V. Sopiha, J. Keller, N. Ross, C. Platzer-Björkman, Germanium Incorporation in $\text{Cu}_2\text{ZnSnS}_4$ and Formation of a Sn–Ge Gradient, *Physica Status Solidi (a)*. 216 (2019) 1900492. <https://doi.org/10.1002/pssa.201900492>.
- [35] E. Garcia-Llamas, J.M. Merino, R. Serna, X. Fontané, I.A. Victorov, A. Pérez-Rodríguez, M. León, I.V. Bodnar, V. Izquierdo-Roca, R. Caballero, Wide band-gap tuning $\text{Cu}_2\text{Sn}_{1-x}\text{Ge}_x\text{S}_4$ single crystals: Optical and vibrational properties, *Solar Energy Materials and Solar Cells*. 158 (2016) 147–153. <https://doi.org/10.1016/j.solmat.2015.12.021>.
- [36] S.M. Sze, *Physics of Semiconductor Devices*, John Wiley & Sons, Ltd, 2006. <https://doi.org/10.1002/9780470068328.ch1>.
- [37] P. Würfel, *Physics of Solar Cells: From Principles to New Concepts*, Third edition, John Wiley & Sons, Ltd, Berlin, 2005. <https://doi.org/10.1002/9783527618545.ch3>.
- [38] K.L. Chopra, S.R. Das, *Thin Film Solar Cells*, 1st ed., Springer US, Boston, MA, 1983. https://doi.org/10.1007/978-1-4899-0418-8_3.
- [39] B. Cullity, *Elements of X-Ray Diffraction* | 3rd edition | Pearson, 3rd ed., n.d. <https://www.pearson.com/store/p/elements-of-x-ray-diffraction/P100000151708/9780201610918> (accessed October 11, 2021).
- [40] N. Bohr, I. On the constitution of atoms and molecules, *Null*. 26 (1913) 1–25. <https://doi.org/10.1080/14786441308634955>.

- [41] R.D.L. Kronig, W.G. Penney, R.H. Fowler, Quantum mechanics of electrons in crystal lattices, *Proceedings of the Royal Society of London. Series A, Containing Papers of a Mathematical and Physical Character*. 130 (1931) 499–513.
<https://doi.org/10.1098/rspa.1931.0019>.
- [42] T. Soga, *Nanostructured Materials for Solar Energy Conversion*, Elsevier, Amsterdam, 2006. <https://doi.org/10.1016/B978-044452844-5/50001-9>.
- [43] W. D Callister, *Materials Science and Engineering: An Introduction*, 10th Edition | Wiley, 10th ed., Wiley, 2018.
<https://www.wiley.com/en-us/Materials+Science+and+Engineering%3A+An+Introduction%2C+10th+Edition-p-9781119405498> (accessed October 1, 2021).
- [44] W. Shockley, H.J. Queisser, Detailed Balance Limit of Efficiency of p-n Junction Solar Cells, *Journal of Applied Physics*. 32 (1961) 510–519. <https://doi.org/10.1063/1.1736034>.
- [45] C.A. Gueymard, D. Myers, K. Emery, Proposed reference irradiance spectra for solar energy systems testing, *Solar Energy*. 73 (2002) 443–467. [https://doi.org/10.1016/S0038-092X\(03\)00005-7](https://doi.org/10.1016/S0038-092X(03)00005-7).
- [46] L. Kocsis, P. Herman, A. Eke, The modified Beer–Lambert law revisited, *Phys. Med. Biol.* 51 (2006) N91–N98.
<https://doi.org/10.1088/0031-9155/51/5/N02>.
- [47] Beer, Bestimmung der Absorption des rothen Lichts in farbigen Flüssigkeiten, *Annalen Der Physik*. 162 (1852) 78–88.
<https://doi.org/10.1002/andp.18521620505>.
- [48] P. Bouguer, *Essai d’optique, sur la gradation de la lumière.*, A Paris : chez Claude Jombert, rue S. Jacques, au coin de la rue des Mathurins, a l’Image Notre-Dame, 1729, 1729. http://archive.org/details/UFIE003101_TO0324_PNI-2703_000000 (accessed October 3, 2021).
- [49] T. Ratz, J.-Y. Raty, G. Brammertz, B. Vermang, N.D. Nguyen, Optoelectronic properties and solar cell efficiency modelling of Cu_2ZnXS_4 ($\text{X} = \text{Sn, Ge, Si}$) kesterites, *J. Phys. Energy*. 3 (2021) 035005.
<https://doi.org/10.1088/2515-7655/abefbe>.
- [50] S. Chen, X.G. Gong, A. Walsh, S.-H. Wei, Electronic structure and stability of quaternary chalcogenide semiconductors derived from cation cross-substitution of II–VI and I–III–VI₂ compounds, *Phys. Rev. B*. 79 (2009) 165211. <https://doi.org/10.1103/PhysRevB.79.165211>.
- [51] P. Reinhard, A. Chirilă, P. Blösch, F. Pianezzi, S. Nishiwaki, S. Buechelers, A.N. Tiwari, Review of progress toward 20% efficiency flexible CIGS solar cells and manufacturing issues of solar modules, in: *2012 IEEE 38th Photovoltaic Specialists Conference (PVSC) PART 2*, 2012: pp. 1–9. <https://doi.org/10.1109/PVSC-Vol2.2012.6656789>.

- [52] M. Johnson, S.V. Baryshev, E. Thimsen, M. Manno, X. Zhang, I.V. Veryovkin, C. Leighton, E.S. Aydil, Alkali-metal-enhanced grain growth in $\text{Cu}_2\text{ZnSnS}_4$ thin films, *Energy Environ. Sci.* 7 (2014) 1931–1938. <https://doi.org/10.1039/C3EE44130J>.
- [53] S. Lopez-Marino, Y. Sanchez, M. Espindola-Rodriguez, X. Alcobe, H. Xie, M. Neuschitzer, I. Becerril, S. Giraldo, M. Dimitrievska, M. Placidi, L. Fourdrinier, V. Izquierdo-Roca, A. Perez-Rodriguez, E. Saucedo, Alkali doping strategies for flexible and light-weight $\text{Cu}_2\text{ZnSnSe}_4$ solar cells, *J. Mater. Chem. A* 4 (2016) 1895–1907. <https://doi.org/10.1039/c5ta09640e>.
- [54] K. Ahn, S.-Y. Kim, S. Kim, D.-H. Son, S.-H. Kim, S. Kim, J. Kim, S.-J. Sung, D.-H. Kim, J.-K. Kang, Flexible high-efficiency CZTSSe solar cells on stainless steel substrates, *Journal of Materials Chemistry A* 7 (2019) 24891–24899. <https://doi.org/10.1039/C9TA08265D>.
- [55] A. Moridi, H. Ruan, L.C. Zhang, M. Liu, Residual stresses in thin film systems: Effects of lattice mismatch, thermal mismatch and interface dislocations, *International Journal of Solids and Structures* 50 (2013) 3562–3569. <https://doi.org/10.1016/j.ijsolstr.2013.06.022>.
- [56] B.N. Chapman, Thin-film adhesion, *Journal of Vacuum Science and Technology* 11 (1974) 106–113. <https://doi.org/10.1116/1.1318537>.
- [57] S. Englund, S. Grini, O. Donzel-Gargand, V. Paneta, V. Kosyak, D. Primetzhofer, J.J.S. Scragg, C. Platzer-Björkman, TiN Interlayers with Varied Thickness in $\text{Cu}_2\text{ZnSnS}(\text{e})_4$ Thin Film Solar Cells: Effect on Na Diffusion, Back Contact Stability, and Performance, *Physica Status Solidi (a)* 215 (2018) 1800491. <https://doi.org/10.1002/pssa.201800491>.
- [58] S. Englund, V. Paneta, D. Primetzhofer, Y. Ren, O. Donzel-Gargand, J.K. Larsen, J. Scragg, C. Platzer Björkman, Characterization of TiN back contact interlayers with varied thickness for $\text{Cu}_2\text{ZnSn}(\text{S,Se})_4$ thin film solar cells, *Thin Solid Films* 639 (2017) 91–97. <https://doi.org/10.1016/j.tsf.2017.08.030>.
- [59] J. Zhou, X. Xu, B. Duan, H. Wu, J. Shi, Y. Luo, D. Li, Q. Meng, Regulating crystal growth via organic lithium salt additive for efficient Kesterite solar cells, *Nano Energy* 89 (2021) 106405. <https://doi.org/10.1016/j.nanoen.2021.106405>.
- [60] M. Kumar, A. Dubey, N. Adhikari, S. Venkatesan, Q. Qiao, Strategic review of secondary phases, defects and defect-complexes in kesterite CZTS–Se solar cells, *Energy & Environmental Science* 8 (2015) 3134–3159. <https://doi.org/10.1039/C5EE02153G>.
- [61] S. Bourdais, C. Choné, B. Delatouche, A. Jacob, G. Larramona, C. Moisan, A. Lafond, F. Donatini, G. Rey, S. Siebentritt, A. Walsh, G. Dennler, Is the Cu/Zn Disorder the Main Culprit for the Voltage Deficit in Kesterite Solar Cells?, *Advanced Energy Materials* 6 (2016) 1502276. <https://doi.org/10.1002/aenm.201502276>.

- [62] S. Giraldo, Z. Jehl, M. Placidi, V. Izquierdo-Roca, A. Pérez-Rodríguez, E. Saucedo, Progress and Perspectives of Thin Film Kesterite Photovoltaic Technology: A Critical Review, *Advanced Materials*. 31 (2019) 1806692. <https://doi.org/10.1002/adma.201806692>.
- [63] S. Hadke, S. Levchenko, G.S. Gautam, C.J. Hages, J.A. Márquez, V. Izquierdo-Roca, E.A. Carter, T. Unold, L.H. Wong, Suppressed Deep Traps and Bandgap Fluctuations in $\text{Cu}_2\text{CdSnS}_4$ Solar Cells with $\approx 8\%$ Efficiency, *Advanced Energy Materials*. 0 (n.d.) 1902509. <https://doi.org/10.1002/aenm.201902509>.
- [64] K. Biswas, S. Lany, A. Zunger, The electronic consequences of multivalent elements in inorganic solar absorbers: Multivalency of Sn in $\text{Cu}_2\text{ZnSnS}_4$, *Applied Physics Letters*. 96 (2010) 201902. <https://doi.org/10.1063/1.3427433>.
- [65] J. Paier, R. Asahi, A. Nagoya, G. Kresse, $\text{Cu}_2\text{ZnSnS}_4$ as a potential photovoltaic material: A hybrid Hartree-Fock density functional theory study, *Phys. Rev. B*. 79 (2009) 115126. <https://doi.org/10.1103/PhysRevB.79.115126>.
- [66] G.M. Ford, Q. Guo, R. Agrawal, H.W. Hillhouse, Earth Abundant Element $\text{Cu}_2\text{Zn}(\text{Sn}_{1-x}\text{Ge}_x)\text{S}_4$ Nanocrystals for Tunable Band Gap Solar Cells: 6.8% Efficient Device Fabrication, *Chem. Mater*. 23 (2011) 2626–2629. <https://doi.org/10.1021/cm2002836>.
- [67] C.J. Hages, S. Levchenko, C.K. Miskin, J.H. Alsmeier, D. Abou-Ras, R.G. Wilks, M. Bär, T. Unold, R. Agrawal, Improved performance of Ge-alloyed CZTGeSSe thin-film solar cells through control of elemental losses, *Progress in Photovoltaics: Research and Applications*. 23 (2015) 376–384. <https://doi.org/10.1002/pip.2442>.
- [68] Q. Guo, G.M. Ford, W.-C. Yang, C.J. Hages, H.W. Hillhouse, R. Agrawal, Enhancing the performance of CZTSSe solar cells with Ge alloying, *Solar Energy Materials and Solar Cells*. 105 (2012) 132–136. <https://doi.org/10.1016/j.solmat.2012.05.039>.
- [69] M. Singh, T.R. Rana, J. Kim, Fabrication of band gap tuned $\text{Cu}_2\text{Zn}(\text{Sn}_{1-x}\text{Ge}_x)(\text{S},\text{Se})_4$ absorber thin film using nanocrystal-based ink in non-toxic solvent, *Journal of Alloys and Compounds*. 675 (2016) 370–376. <https://doi.org/10.1016/j.jallcom.2016.03.138>.
- [70] M. Umehara, S. Tajima, Y. Takeda, T. Motohiro, Wide bandgap $\text{Cu}_2\text{ZnSn}_{1-x}\text{Ge}_x\text{S}_4$ fabricated on transparent conductive oxide-coated substrates for top-cells of multi-junction solar cells, *Journal of Alloys and Compounds*. 689 (2016) 713–717. <https://doi.org/10.1016/j.jallcom.2016.08.039>.
- [71] A.D. Adewoyin, M.A. Olopade, O.O. Oyebola, M.A. Chendo, Development of CZTGS/CZTS tandem thin film solar cell using SCAPS-1D, *Optik*. 176 (2019) 132–142. <https://doi.org/10.1016/j.ijleo.2018.09.033>.

- [72] T.G. Sanchez, E. Regalado-Pérez, X. Mathew, M.F. Sanchez, Y. Sanchez, E. Saucedo, N.R. Mathews, Ge doped $\text{Cu}_2\text{ZnSnS}_4$: An investigation on absorber recrystallization and opto-electronic properties of solar cell, *Solar Energy Materials and Solar Cells*. 198 (2019) 44–52. <https://doi.org/10.1016/j.solmat.2019.04.011>.
- [73] K.-S. Lim, S.-M. Yu, S. Seo, H. Shin, T.-S. Oh, J.-B. Yoo, Incorporation of Ge in $\text{Cu}_2\text{ZnSnS}_4$ thin film in a Zn-poor composition range, *Materials Science in Semiconductor Processing*. 89 (2019) 194–200. <https://doi.org/10.1016/j.mssp.2018.09.020>.
- [74] I. Kim, K. Kim, Y. Oh, K. Woo, G. Cao, S. Jeong, J. Moon, Bandgap-Graded $\text{Cu}_2\text{Zn}(\text{Sn}_{1-x}\text{Ge}_x)\text{S}_4$ Thin-Film Solar Cells Derived from Metal Chalcogenide Complex Ligand Capped Nanocrystals, *Chemistry of Materials*. 26 (2014) 3957–3965. <https://doi.org/10.1021/cm501568d>.
- [75] J. Just, M. Nichterwitz, D. Lützenkirchen-Hecht, R. Frahm, T. Unold, Compositional dependence of charge carrier transport in kesterite $\text{Cu}_2\text{ZnSnS}_4$ solar cells, *Journal of Applied Physics*. 120 (2016) 225703. <https://doi.org/10.1063/1.4971179>.
- [76] C. Frisk, Y. Ren, Shuyi Li, C. Platzer-Björkman, CZTS solar cell device simulations with varying absorber thickness, in: 2015 IEEE 42nd Photovoltaic Specialist Conference (PVSC), 2015: pp. 1–3. <https://doi.org/10.1109/PVSC.2015.7355794>.
- [77] Y.S. Lee, T. Gershon, O. Gunawan, T.K. Todorov, T. Gokmen, Y. Virgus, S. Guha, $\text{Cu}_2\text{ZnSnSe}_4$ Thin-Film Solar Cells by Thermal Co-evaporation with 11.6% Efficiency and Improved Minority Carrier Diffusion Length, *Advanced Energy Materials*. 5 (2015) 1401372. <https://doi.org/10.1002/aenm.201401372>.
- [78] B. Shin, O. Gunawan, Y. Zhu, N.A. Bojarczuk, S.J. Chey, S. Guha, Thin film solar cell with 8.4% power conversion efficiency using an earth-abundant $\text{Cu}_2\text{ZnSnS}_4$ absorber, *Progress in Photovoltaics: Research and Applications*. 21 (2013) 72–76. <https://doi.org/10.1002/pip.1174>.
- [79] F. Liu, C. Yan, J. Huang, K. Sun, F. Zhou, J.A. Stride, M.A. Green, X. Hao, Nanoscale Microstructure and Chemistry of $\text{Cu}_2\text{ZnSnS}_4/\text{CdS}$ Interface in Kesterite $\text{Cu}_2\text{ZnSnS}_4$ Solar Cells, *Advanced Energy Materials*. 6 (2016) 1600706. <https://doi.org/10.1002/aenm.201600706>.
- [80] G. Brammertz, S. Oueslati, M. Buffière, J. Bekaert, H. El Anzeery, K.B. Messaoud, S. Sahayaraj, T. Nuytten, C. Köble, M. Meuris, J. Poortmans, Investigation of Properties Limiting Efficiency in $\text{Cu}_2\text{ZnSnSe}_4$ -Based Solar Cells, *IEEE Journal of Photovoltaics*. 5 (2015) 649–655. <https://doi.org/10.1109/JPHOTOV.2014.2376053>.
- [81] S. Giraldo, E. Saucedo, M. Neuschitzer, F. Oliva, M. Placidi, X. Alcobé, V. Izquierdo-Roca, S. Kim, H. Tampo, H. Shibata, A. Pérez-Rodríguez, P. Pistor, How small amounts of Ge modify the formation

- pathways and crystallization of kesterites, *Energy Environ. Sci.* 11 (2018) 582–593. <https://doi.org/10.1039/C7EE02318A>.
- [82] A.D. Collord, H.W. Hillhouse, Germanium Alloyed Kesterite Solar Cells with Low Voltage Deficits, *Chem. Mater.* 28 (2016) 2067–2073. <https://doi.org/10.1021/acs.chemmater.5b04806>.
- [83] S. Kim, K.M. Kim, H. Tampo, H. Shibata, S. Niki, Improvement of voltage deficit of Ge-incorporated kesterite solar cell with 12.3% conversion efficiency, *Applied Physics Express*. 9 (2016) 102301. <https://doi.org/10.7567/APEX.9.102301>.
- [84] T. Ericson, F. Larsson, T. Törndahl, C. Frisk, J. Larsen, V. Kosyak, C. Hägglund, S. Li, C. Platzer-Björkman, Zinc-Tin-Oxide Buffer Layer and Low Temperature Post Annealing Resulting in a 9.0% Efficient Cd-Free $\text{Cu}_2\text{ZnSnS}_4$ Solar Cell, *Solar RRL*. 1 (2017) 1700001. <https://doi.org/10.1002/solr.201700001>.
- [85] K. Tsuji, T. Maeda, T. Wada, Optical properties and electronic structures of $\text{Cu}_2\text{ZnSnS}_4$, $\text{Cu}_2\text{ZnGeS}_4$, and $\text{Cu}_2\text{Zn}(\text{Ge},\text{Sn})\text{S}_4$ and $\text{Cu}_2\text{Zn}(\text{Ge},\text{Sn})\text{Se}_4$ solid solutions, *Jpn. J. Appl. Phys.* 57 (2018) 08RC21. <https://doi.org/10.7567/JJAP.57.08RC21>.
- [86] S. Levchenko, M. Guc, C. Merschjann, G. Gurieva, S. Schorr, M. Lux-Steiner, E. Arushanov, Photoluminescence characterization of $\text{Cu}_2\text{ZnGeS}_4$ single crystals, *Physica Status Solidi c*. 10 (2013) 1079–1081. <https://doi.org/10.1002/pssc.201200843>.
- [87] J. Márquez, H. Stange, C.J. Hages, N. Schaefer, S. Levchenko, S. Giraldo, E. Saucedo, K. Schwarzburg, D. Abou-Ras, A. Redinger, M. Klaus, C. Genzel, T. Unold, R. Mainz, Chemistry and Dynamics of Ge in Kesterite: Toward Band-Gap-Graded Absorbers, *Chem. Mater.* 29 (2017) 9399–9406. <https://doi.org/10.1021/acs.chemmater.7b03416>.
- [88] B. Vermang, Y. Ren, O. Donzel-Gargand, C. Frisk, J. Joel, P. Salomé, J. Borme, S. Sadewasser, C. Platzer-Björkman, M. Edoff, Rear Surface Optimization of CZTS Solar Cells by Use of a Passivation Layer With Nanosized Point Openings, *IEEE Journal of Photovoltaics*. 6 (2016) 332–336. <https://doi.org/10.1109/JPHOTOV.2015.2496864>.
- [89] S. Bose, J.M.V. Cunha, S. Suresh, J.D. Wild, T.S. Lopes, J.R.S. Barbosa, R. Silva, J. Borme, P.A. Fernandes, B. Vermang, P.M.P. Salomé, Optical Lithography Patterning of SiO_2 Layers for Interface Passivation of Thin Film Solar Cells, *Solar RRL*. 2 (2018) 1800212. <https://doi.org/10.1002/solr.201800212>.
- [90] J.F. Geisz, R.M. France, K.L. Schulte, M.A. Steiner, A.G. Norman, H.L. Guthrey, M.R. Young, T. Song, T. Moriarty, Six-junction III–V solar cells with 47.1% conversion efficiency under 143 Suns concentration, *Nat Energy*. 5 (2020) 326–335. <https://doi.org/10.1038/s41560-020-0598-5>.

- [91] A. Hajijafarassar, F. Martinho, F. Stulen, S. Grini, S. López-Mariño, M. Espíndola-Rodríguez, M. Döbeli, S. Canulescu, E. Stamate, M. Gansukh, S. Engberg, A. Crovetto, L. Vines, J. Schou, O. Hansen, Monolithic thin-film chalcogenide–silicon tandem solar cells enabled by a diffusion barrier, *Solar Energy Materials and Solar Cells*. 207 (2020) 110334. <https://doi.org/10.1016/j.solmat.2019.110334>.
- [92] K. Sun, C. Yan, J. Huang, K. Sun, H. Sun, L. Jiang, X. Deng, J. Stride, X. Hao, F. Liu, Minority lifetime and efficiency improvement for CZTS solar cells via Cd ion soaking and post treatment, *Journal of Alloys and Compounds*. 750 (2018) 328–332. <https://doi.org/10.1016/j.jallcom.2018.03.401>.
- [93] S. Siebentritt, Why are kesterite solar cells not 20% efficient?, *Thin Solid Films*. 535 (2013) 1–4. <https://doi.org/10.1016/j.tsf.2012.12.089>.
- [94] A. Santoni, F. Biccari, C. Malerba, M. Valentini, R. Chierchia, A. Mittiga, Valence band offset at the CdS/Cu₂ZnSnS₄ interface probed by x-ray photoelectron spectroscopy, *J. Phys. D: Appl. Phys.* 46 (2013) 175101. <https://doi.org/10.1088/0022-3727/46/17/175101>.
- [95] M. Neuschitzer, K. Lienau, M. Guc, L.C. Barrio, S. Haass, J.M. Prieto, Y. Sanchez, M. Espindola-Rodriguez, Y. Romanyuk, A. Perez-Rodriguez, V. Izquierdo-Roca, E. Saucedo, Towards high performance Cd-free CZTSe solar cells with a ZnS(O,OH) buffer layer: the influence of thiourea concentration on chemical bath deposition, *J. Phys. D: Appl. Phys.* 49 (2016) 125602. <https://doi.org/10.1088/0022-3727/49/12/125602>.
- [96] C. Platzer-Björkman, N. Barreau, M. Bär, L. Choubrac, L. Grenet, J. Heo, T. Kubart, A. Mittiga, Y. Sanchez, J. Scragg, S. Sinha, M. Valentini, Back and front contacts in kesterite solar cells: state-of-the-art and open questions, *J. Phys. Energy*. 1 (2019) 044005. <https://doi.org/10.1088/2515-7655/ab3708>.
- [97] J. Kim, C. Park, S.M. Pawar, A.I. Inamdar, Y. Jo, J. Han, J. Hong, Y.S. Park, D.-Y. Kim, W. Jung, H. Kim, H. Im, Optimization of sputtered ZnS buffer for Cu₂ZnSnS₄ thin film solar cells, *Thin Solid Films*. 566 (2014) 88–92. <https://doi.org/10.1016/j.tsf.2014.07.024>.
- [98] D. Hiraniwa, N. Matsuo, N. Sakai, T. Katou, H. Sugimoto, J. Chantana, Z. Tang, T. Minemoto, Sputtered (Zn,Mg)O buffer layer for band offset control in Cu₂ZnSn(S,Se)₄ solar cells, *Jpn. J. Appl. Phys.* 53 (2014) 106502. <https://doi.org/10.7567/JJAP.53.106502>.
- [99] D.A.R. Barkhouse, R. Haight, N. Sakai, H. Hiroi, H. Sugimoto, D.B. Mitzi, Cd-free buffer layer materials on Cu₂ZnSn(S_xSe_{1-x})₄: Band alignments with ZnO, ZnS, and In₂S₃, *Appl. Phys. Lett.* 100 (2012) 193904. <https://doi.org/10.1063/1.4714737>.
- [100] S. Siol, T.P. Dhakal, G.S. Gudavalli, P.P. Rajbhandari, C. DeHart, L.L. Baranowski, A. Zakutayev, Combinatorial Reactive Sputtering of In₂S₃ as an Alternative Contact Layer for Thin Film Solar Cells,

- ACS Appl. Mater. Interfaces. 8 (2016) 14004–14011.
<https://doi.org/10.1021/acsami.6b02213>.
- [101] C. Agashe, O. Kluth, J. Hüpkes, U. Zastrow, B. Rech, M. Wuttig, Efforts to improve carrier mobility in radio frequency sputtered aluminum doped zinc oxide films, *Journal of Applied Physics*. 95 (2004) 1911–1917. <https://doi.org/10.1063/1.1641524>.
 - [102] J. Müller, B. Rech, J. Springer, M. Vanecek, TCO and light trapping in silicon thin film solar cells, *Solar Energy*. 77 (2004) 917–930. <https://doi.org/10.1016/j.solener.2004.03.015>.
 - [103] H. Hartnagel, A. Hartnagel, A.L. Dawar, C. Jagadish, A.K. Jain, *Semiconducting Transparent Thin Films*, Taylor & Francis, 1995.
 - [104] S. Englund, Alternative back contacts for CZTS thin film solar cells, Uppsala University, 2020. <http://urn.kb.se/resolve?urn=urn:nbn:se:uu:diva-403583> (accessed August 13, 2020).
 - [105] C. Platzer-Björkman, J. Scragg, H. Flammersberger, T. Kubart, M. Edoff, Influence of precursor sulfur content on film formation and compositional changes in $\text{Cu}_2\text{ZnSnS}_4$ films and solar cells, *Solar Energy Materials and Solar Cells*. 98 (2012) 110–117. <https://doi.org/10.1016/j.solmat.2011.10.019>.
 - [106] J.J. Scragg, T. Ericson, T. Kubart, M. Edoff, C. Platzer-Björkman, Chemical Insights into the Instability of $\text{Cu}_2\text{ZnSnS}_4$ Films during Annealing, *Chem. Mater.* 23 (2011) 4625–4633. <https://doi.org/10.1021/cm202379s>.
 - [107] P.M.P. Salomé, V. Fjallstrom, A. Hultqvist, P. Szaniawski, U. Zimmermann, M. Edoff, The effect of Mo back contact ageing on $\text{Cu}(\text{In,Ga})\text{Se}_2$ thin-film solar cells, *Progress in Photovoltaics: Research and Applications*. 22 (2014) 83–89. <https://doi.org/10.1002/pip.2360>.
 - [108] Y. Ren, J.J.S. Scragg, M. Edoff, J.K. Larsen, C. Platzer-Björkman, Evolution of Na-S(-O) Compounds on the $\text{Cu}_2\text{ZnSnS}_4$ Absorber Surface and Their Effects on CdS Thin Film Growth, *ACS Appl. Mater. Interfaces*. 8 (2016) 18600–18607. <https://doi.org/10.1021/acsami.6b04978>.
 - [109] P.O. Oviroh, R. Akbarzadeh, D. Pan, R.A.M. Coetzee, T.-C. Jen, New development of atomic layer deposition: processes, methods and applications, *Science and Technology of Advanced Materials*. 20 (2019) 465–496. <https://doi.org/10.1080/14686996.2019.1599694>.
 - [110] F. Larsson, Window Layer Structures for Chalcopyrite Thin-Film Solar Cells, (2020). <http://urn.kb.se/resolve?urn=urn:nbn:se:uu:diva-416751> (accessed October 21, 2021).
 - [111] J. Lindahl, J. Keller, O. Donzel-Gargand, P. Szaniawski, M. Edoff, T. Törndahl, Deposition temperature induced conduction band changes in zinc tin oxide buffer layers for $\text{Cu}(\text{In,Ga})\text{Se}_2$ solar cells, *Solar Energy Materials and Solar Cells*. 144 (2016) 684–690. <https://doi.org/10.1016/j.solmat.2015.09.048>.

- [112] J. Lindahl, U. Zimmermann, P. Szaniawski, T. Torndahl, A. Hultqvist, P. Salome, C. Platzer-Bjorkman, M. Edoff, Inline Cu(In,Ga)Se₂ Co-evaporation for High-Efficiency Solar Cells and Modules, *IEEE Journal of Photovoltaics*. 3 (2013) 1100–1105. <https://doi.org/10.1109/JPHOTOV.2013.2256232>.
- [113] T. Ericson, Sputtering of Precursors for Cu₂ZnSnS₄ Solar Cells and Application of Cadmium Free Buffer Layers, Uppsala University. (2018). <http://urn.kb.se/resolve?urn=urn:nbn:se:uu:diva-357354> (accessed August 13, 2020).
- [114] K.W. Kho, U.S. Dinish, M. Olivo, 5 - Biomedicine with surface enhanced Raman scattering (SERS), in: I. Meglinski (Ed.), *Biophotonics for Medical Applications*, Woodhead Publishing, 2015: pp. 101–134. <https://doi.org/10.1016/B978-0-85709-662-3.00005-1>.
- [115] E.V. Efremov, F. Ariese, C. Gooijer, Achievements in resonance Raman spectroscopy: Review of a technique with a distinct analytical chemistry potential, *Analytica Chimica Acta*. 606 (2008) 119–134. <https://doi.org/10.1016/j.aca.2007.11.006>.
- [116] J.J.S. Scragg, J.K. Larsen, M. Kumar, C. Persson, J. Sendler, S. Siebentritt, C.P. Björkman, Cu–Zn disorder and band gap fluctuations in Cu₂ZnSn(S,Se)₄: Theoretical and experimental investigations, *Physica Status Solidi (b)*. 253 (2016) 247–254. <https://doi.org/10.1002/pssb.201552530>.
- [117] W.Q. Hong, Extraction of extinction coefficient of weak absorbing thin films from special absorption, *J. Phys. D: Appl. Phys.* 22 (1989) 1384–1385. <https://doi.org/10.1088/0022-3727/22/9/024>.
- [118] J. Tauc, Optical properties and electronic structure of amorphous Ge and Si, *Materials Research Bulletin*. 3 (1968) 37–46. [https://doi.org/10.1016/0025-5408\(68\)90023-8](https://doi.org/10.1016/0025-5408(68)90023-8).
- [119] P. Małucha, M. Pacia, W. Macyk, How To Correctly Determine the Band Gap Energy of Modified Semiconductor Photocatalysts Based on UV–Vis Spectra, *J. Phys. Chem. Lett.* 9 (2018) 6814–6817. <https://doi.org/10.1021/acs.jpcclett.8b02892>.
- [120] D.B. Williams, C.B. Carter, The Transmission Electron Microscope, in: D.B. Williams, C.B. Carter (Eds.), *Transmission Electron Microscopy: A Textbook for Materials Science*, Springer US, Boston, MA, 1996: pp. 3–17. https://doi.org/10.1007/978-1-4757-2519-3_1.
- [121] A. Mayoral, J.E. Readman, P.A. Anderson, Aberration-Corrected STEM Analysis of a Cubic Cd Array Encapsulated in Zeolite A, *J. Phys. Chem. C*. 117 (2013) 24485–24489. <https://doi.org/10.1021/jp409171q>.
- [122] S.S. Hegedus, W.N. Shafarman, Thin-film solar cells: device measurements and analysis, *Progress in Photovoltaics: Research and Applications*. 12 (2004) 155–176. <https://doi.org/10.1002/pip.518>.

- [123] K. Doverspike, K. Dwight, A. Wold, Preparation and characterization of copper zinc germanium sulfide selenide ($\text{Cu}_2\text{ZnGeS}_{4-y}\text{Se}_y$), *Chem. Mater.* 2 (1990) 194–197. <https://doi.org/10.1021/cm00008a023>.
- [124] C.-M. Fan, M.D. Regulacio, C. Ye, S.H. Lim, S.K. Lua, Q.-H. Xu, Z. Dong, A.-W. Xu, M.-Y. Han, Colloidal nanocrystals of orthorhombic $\text{Cu}_2\text{ZnGeS}_4$: phase-controlled synthesis, formation mechanism and photocatalytic behavior, *Nanoscale*. 7 (2015) 3247–3253. <https://doi.org/10.1039/C4NR07012G>.
- [125] M.E. Norako, R.L. Brutchey, Synthesis of Metastable Wurtzite CuInSe_2 Nanocrystals, *Chem. Mater.* 22 (2010) 1613–1615. <https://doi.org/10.1021/cm100341r>.
- [126] D. Mora-Herrera, M. Pal, F. Paraguay-Delgado, Facile solvothermal synthesis of $\text{Cu}_2\text{ZnSn}_{1-x}\text{Ge}_x\text{S}_4$ nanocrystals: Effect of Ge content on optical and electrical properties, *Materials Chemistry and Physics*. 257 (2021) 123764. <https://doi.org/10.1016/j.matchemphys.2020.123764>.
- [127] A.M. Holder, S. Siol, P.F. Ndione, H. Peng, A.M. Deml, B.E. Matthews, L.T. Schelhas, M.F. Toney, R.G. Gordon, W. Tumas, J.D. Perkins, D.S. Ginley, B.P. Gorman, J. Tate, A. Zakutayev, S. Lany, Novel phase diagram behavior and materials design in heterostructural semiconductor alloys, *Science Advances*. 3 (2017) e1700270. <https://doi.org/10.1126/sciadv.1700270>.
- [128] X. Wen, W. Luo, Z. Guan, W. Huang, Z. Zou, Boosting efficiency and stability of a $\text{Cu}_2\text{ZnSnS}_4$ photocathode by alloying Ge and increasing sulfur pressure simultaneously, *Nano Energy*. 41 (2017) 18–26. <https://doi.org/10.1016/j.nanoen.2017.09.006>.
- [129] J. Fu, D. Kou, W. Zhou, Z. Zhou, S. Yuan, Y. Qi, S. Wu, Ag, Ge dual-gradient substitution for low-energy loss and high-efficiency kesterite solar cells, *J. Mater. Chem. A*. 8 (2020) 22292–22301. <https://doi.org/10.1039/D0TA06318E>.
- [130] C. Andres, A. Cabas-Vidani, A.N. Tiwari, Y.E. Romanyuk, From sputtered metal precursors towards $\text{Cu}_2\text{Zn}(\text{Sn}_{1-x}\text{Ge}_x)\text{Se}_4$ thin film solar cells with shallow back grading, *Thin Solid Films*. 665 (2018) 168–172. <https://doi.org/10.1016/j.tsf.2018.09.022>.
- [131] A.H. Munshi, J. Kephart, A. Abbas, J. Raguse, J.-N. Beaudry, K. Barth, J. Sites, J. Walls, W. Sampath, Polycrystalline CdSeTe/CdTe Absorber Cells With 28 mA/cm^2 Short-Circuit Current, *IEEE Journal of Photovoltaics*. 8 (2018) 310–314. <https://doi.org/10.1109/JPHOTOV.2017.2775139>.
- [132] O. Lundberg, M. Bodegård, J. Malmström, L. Stolt, Influence of the $\text{Cu}(\text{In,Ga})\text{Se}_2$ thickness and Ga grading on solar cell performance, *Progress in Photovoltaics: Research and Applications*. 11 (2003) 77–88. <https://doi.org/10.1002/pip.462>.

- [133] J. Li, D. Wang, X. Li, Y. Zeng, Y. Zhang, Cation Substitution in Earth-Abundant Kesterite Photovoltaic Materials, *Advanced Science*. 5 (2018) 1700744. <https://doi.org/10.1002/advs.201700744>.
- [134] S. Kermadi, S. Sali, L. Zougar, M. Boumaour, R. Gunder, S. Schorr, V. Izquierdo-Roca, A. Pérez-Rodríguez, An in-depth investigation on the grain growth and the formation of secondary phases of ultrasonic-sprayed $\text{Cu}_2\text{ZnSnS}_4$ based thin films assisted by Na crystallization catalyst, *Solar Energy*. 176 (2018) 277–286. <https://doi.org/10.1016/j.solener.2018.10.045>.
- [135] L.G. Harrison, Influence of dislocations on diffusion kinetics in solids with particular reference to the alkali halides, *Trans. Faraday Soc.* 57 (1961) 1191–1199. <https://doi.org/10.1039/TF9615701191>.
- [136] P.A. Fernandes, P.M.P. Salomé, A.F. da Cunha, Study of polycrystalline $\text{Cu}_2\text{ZnSnS}_4$ films by Raman scattering, *Journal of Alloys and Compounds*. 509 (2011) 7600–7606. <https://doi.org/10.1016/j.jall-com.2011.04.097>.
- [137] X. Fontané, L. Calvo-Barrio, V. Izquierdo-Roca, E. Saucedo, A. Pérez-Rodríguez, J.R. Morante, D.M. Berg, P.J. Dale, S. Siebentritt, In-depth resolved Raman scattering analysis for the identification of secondary phases: Characterization of $\text{Cu}_2\text{ZnSnS}_4$ layers for solar cell applications, *Appl. Phys. Lett.* 98 (2011) 181905. <https://doi.org/10.1063/1.3587614>.
- [138] J. Just, C. M. Sutter-Fella, D. Lützenkirchen-Hecht, R. Frahm, S. Schorr, T. Unold, Secondary phases and their influence on the composition of the kesterite phase in CZTS and CZTSe thin films, *Physical Chemistry Chemical Physics*. 18 (2016) 15988–15994. <https://doi.org/10.1039/C6CP00178E>.
- [139] J.J. Scragg, J.T. Wätjen, M. Edoff, T. Ericson, T. Kubart, C. Platzer-Björkman, A Detrimental Reaction at the Molybdenum Back Contact in $\text{Cu}_2\text{ZnSn}(\text{S},\text{Se})_4$ Thin-Film Solar Cells, *J. Am. Chem. Soc.* 134 (2012) 19330–19333. <https://doi.org/10.1021/ja308862n>.
- [140] D. Nam, S. Cho, J.-H. Sim, K.-J. Yang, D.-H. Son, D.-H. Kim, J.-K. Kang, M.-S. Kwon, C.-W. Jeon, H. Cheong, Solar conversion efficiency and distribution of ZnS secondary phase in $\text{Cu}_2\text{ZnSnS}_4$ solar cells, *Solar Energy Materials and Solar Cells*. 149 (2016) 226–231. <https://doi.org/10.1016/j.solmat.2016.01.025>.
- [141] C.M. Yoon, I.-K. Oh, Y. Lee, J.-G. Song, S.J. Lee, J.-M. Myoung, H.G. Kim, H.-S. Moon, B. Shong, H.-B.-R. Lee, H. Kim, Water-Erasable Memory Device for Security Applications Prepared by the Atomic Layer Deposition of GeO_2 , *Chem. Mater.* 30 (2018) 830–840. <https://doi.org/10.1021/acs.chemmater.7b04371>.
- [142] M.K. Murthy, H. Hill, Studies in Germanium Oxide Systems: III, Solubility of Germania in Water, *Journal of the American Ceramic Society*. 48 (1965) 109–110. <https://doi.org/10.1111/j.1151-2916.1965.tb11811.x>.

- [143] N. Saini, J.K. Larsen, K. Lindgren, A. Fazi, C. Platzer-Björkman, Bandgap engineered $\text{Cu}_2\text{ZnGe}_x\text{Sn}_{1-x}\text{S}_4$ solar cells using an adhesive TiN back contact layer, *Journal of Alloys and Compounds*. 880 (2021) 160478. <https://doi.org/10.1016/j.jallcom.2021.160478>.
- [144] C. Malerba, M. Valentini, A. Mittiga, Cation Disorder In $\text{Cu}_2\text{ZnSnS}_4$ Thin Films: Effect On Solar Cell Performances, *Solar RRL*. 1 (2017) 1700101. <https://doi.org/10.1002/solr.201700101>.
- [145] F. Martinho, A. Hajijafarassar, S. Lopez-Marino, M. Espíndola-Rodríguez, S. Engberg, M. Gansukh, F. Stulen, S. Grini, S. Canulescu, E. Stamate, A. Crovetto, L. Vines, J. Schou, O. Hansen, Nitride-Based Interfacial Layers for Monolithic Tandem Integration of New Solar Energy Materials on Si: The Case of CZTS, *ACS Appl. Energy Mater.* 3 (2020) 4600–4609. <https://doi.org/10.1021/acsam.0c00280>.
- [146] D. Schuldis, A. Richter, J. Benick, P. Saint-Cast, M. Hermle, S.W. Glunz, Properties of the c-Si/ Al_2O_3 interface of ultrathin atomic layer deposited Al_2O_3 layers capped by SiN_x for c-Si surface passivation, *Appl. Phys. Lett.* (2014) 6.
- [147] G. Dingemans, R. Seguin, P. Engelhart, M.C.M. van de Sanden, W.M.M. Kessels, Silicon surface passivation by ultrathin Al_2O_3 films synthesized by thermal and plasma atomic layer deposition, *Physica Status Solidi (RRL) – Rapid Research Letters*. 4 (2010) 10–12. <https://doi.org/10.1002/pssr.200903334>.
- [148] X. Cui, K. Sun, J. Huang, J.S. Yun, C.-Y. Lee, C. Yan, H. Sun, Y. Zhang, C. Xue, K. Eder, L. Yang, J.M. Cairney, J. Seidel, N.J. Ekins-Daukes, M. Green, B. Hoex, X. Hao, Cd-Free $\text{Cu}_2\text{ZnSnS}_4$ solar cell with an efficiency greater than 10% enabled by Al_2O_3 passivation layers, *Energy Environ. Sci.* 12 (2019) 2751–2764. <https://doi.org/10.1039/C9EE01726G>.
- [149] F. Werner, B. Veith, D. Zielke, L. Kühnemund, C. Tegenkamp, M. Seibt, R. Brendel, J. Schmidt, Electronic and chemical properties of the c-Si/ Al_2O_3 interface, *Journal of Applied Physics*. 109 (2011) 113701. <https://doi.org/10.1063/1.3587227>.
- [150] C.-Y. Lee, S. Wang, X. Cui, T. Zhang, R. Deng, K.T. Khoo, B. Hoex, Improving the Silicon Surface Passivation by Aluminum Oxide Grown Using a Non-Pyrophoric Aluminum Precursor, *Physica Status Solidi (RRL) – Rapid Research Letters*. 12 (2018) 1800156. <https://doi.org/10.1002/pssr.201800156>.
- [151] B. Hoex, J. Schmidt, R. Bock, P.P. Altermatt, M.C.M. van de Sanden, W.M.M. Kessels, Excellent passivation of highly doped p-type Si surfaces by the negative-charge-dielectric Al_2O_3 , *Appl. Phys. Lett.* 91 (2007) 112107. <https://doi.org/10.1063/1.2784168>.

- [152] J.M. Kephart, A. Kindvall, D. Williams, D. Kuciauskas, P. Dippo, A. Munshi, W.S. Sampath, Sputter-Deposited Oxides for Interface Passivation of CdTe Photovoltaics, *IEEE Journal of Photovoltaics*. 8 (2018) 587–593. <https://doi.org/10.1109/JPHOTOV.2017.2787021>.
- [153] F. Liu, J. Huang, K. Sun, C. Yan, Y. Shen, J. Park, A. Pu, F. Zhou, X. Liu, J.A. Stride, M.A. Green, X. Hao, Beyond 8% ultrathin kesterite $\text{Cu}_2\text{ZnSnS}_4$ solar cells by interface reaction route controlling and self-organized nanopattern at the back contact, *NPG Asia Mater.* 9 (2017) e401–e401. <https://doi.org/10.1038/am.2017.103>.
- [154] J. Kim, S. Park, S. Ryu, J. Oh, B. Shin, Improving the open-circuit voltage of $\text{Cu}_2\text{ZnSnSe}_4$ thin film solar cells via interface passivation, *Progress in Photovoltaics: Research and Applications*. 25 (2017) 308–317. <https://doi.org/10.1002/pip.2864>.
- [155] Y.S. Lee, T. Gershon, T.K. Todorov, W. Wang, M.T. Winkler, M. Hopstaken, O. Gunawan, J. Kim, Atomic Layer Deposited Aluminum Oxide for Interface Passivation of $\text{Cu}_2\text{ZnSn}(\text{S},\text{Se})_4$ Thin-Film Solar Cells, *Advanced Energy Materials*. 6 (2016) 1600198. <https://doi.org/10.1002/aenm.201600198>.
- [156] B. Vermang, V. Fjällström, X. Gao, M. Edoff, Improved Rear Surface Passivation of $\text{Cu}(\text{In},\text{Ga})\text{Se}_2$ Solar Cells: A Combination of an Al_2O_3 Rear Surface Passivation Layer and Nanosized Local Rear Point Contacts, *IEEE Journal of Photovoltaics*. 4 (2014) 486–492. <https://doi.org/10.1109/JPHOTOV.2013.2287769>.
- [157] P. Saint-Cast, D. Kania, M. Hofmann, J. Benick, J. Rentsch, R. Preu, Very low surface recombination velocity on p-type c-Si by high-rate plasma-deposited aluminum oxide, *Appl. Phys. Lett.* 95 (2009) 151502. <https://doi.org/10.1063/1.3250157>.
- [158] B. Vermang, Y. Ren, O. Donzel-Gargand, C. Frisk, J. Joel, P. Salomé, J. Borme, S. Sadewasser, C. Platzer-Björkman, M. Edoff, Rear Surface Optimization of CZTS Solar Cells by Use of a Passivation Layer With Nanosized Point Openings, *IEEE Journal of Photovoltaics*. 6 (2016) 332–336. <https://doi.org/10.1109/JPHOTOV.2015.2496864>.
- [159] S.-Y. Kim, S.-H. Kim, S. Hong, D.-H. Son, Y.-I. Kim, S. Kim, K. Ahn, K.-J. Yang, D.-H. Kim, J.-K. Kang, Secondary Phase Formation Mechanism in the Mo-Back Contact Region during Sulfo-Selenization Using a Metal Precursor: Effect of Wettability between a Liquid Metal and Substrate on Secondary Phase Formation, *ACS Appl. Mater. Interfaces*. 11 (2019) 23160–23167. <https://doi.org/10.1021/acsami.9b03969>.

Acta Universitatis Upsaliensis

*Digital Comprehensive Summaries of Uppsala Dissertations
from the Faculty of Science and Technology 2086*

Editor: The Dean of the Faculty of Science and Technology

A doctoral dissertation from the Faculty of Science and Technology, Uppsala University, is usually a summary of a number of papers. A few copies of the complete dissertation are kept at major Swedish research libraries, while the summary alone is distributed internationally through the series Digital Comprehensive Summaries of Uppsala Dissertations from the Faculty of Science and Technology. (Prior to January, 2005, the series was published under the title "Comprehensive Summaries of Uppsala Dissertations from the Faculty of Science and Technology".)



ACTA
UNIVERSITATIS
UPSALIENSIS
UPPSALA
2021

Distribution: publications.uu.se
urn:nbn:se:uu:diva-456779